ACSNANO

www.acsnano.org

ARTICLE

Single-Particle Studies Reveal a Nanoscale Mechanism for Elastic, Bright, and Repeatable ZnS:Mn Mechanoluminescence in a Low-Pressure Regime

Maria V. Mukhina,* Jason Tresback, Justin C. Ondry, Austin Akey, A. Paul Alivisatos, and Nancy Kleckner*

Cite This: *ACS Nano* 2021, 15, 4115−4133

Read Online

ACCESS | Metrics & More | Article Recommendations | Supporting Information

ABSTRACT: Mechanoluminescent materials, which emit light in response to elastic deformation, are demanded for use as *in situ* stress sensors. ZnS doped with Mn is known to exhibit one of the lowest reported thresholds for appearance of mechanoluminescence, with repeatable light emission under contact pressure <10 MPa. The physical basis for such behavior remains as yet unclear. Here, reliable microscopic detection of mechanoluminescence of single ZnS:Mn microparticles, in combination with nanoscale structural characterization, provides evidence that the mechanoluminescent properties of these particles result from interplay between a non-centrosymmetric crystal lattice and its defects, *viz.*, dislocations and stacking faults. Statistical analysis of the distributions of mechanoluminescence energy release trajectories reveals two distinct mechanisms of excitation: one attributable to a piezo-phototronic effect and the other due to dislocation motion. At pressures below 8.1 MPa, both mechanisms contribute to mechanoluminescent output, with a dominant contribution from the piezo-phototronic mechanism. In contrast, above 8.1 MPa, dislocation motion is the primary excitation source. For the piezo-phototronic mechanism, we propose a specific model that accounts for elastic ZnS:Mn mechanoluminescence under very low pressure. The charged interfaces in stacking faults lead to the presence of filled traps, which otherwise would be empty in the absence of the built-in electric field. Upon application of external stress, local enhancement of the piezoelectric field at the stacking faults' interfaces facilitates release of the trapped carriers and subsequent luminescence. This field enhancement explains how <10 MPa pressure produces thousands of photons.

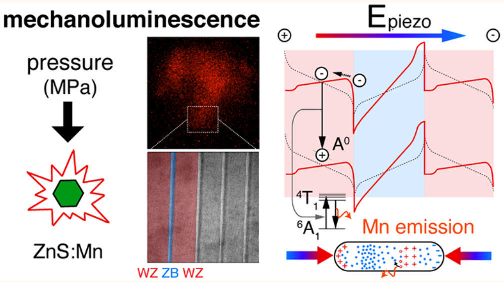

KEYWORDS: *elastic mechanoluminescence, single-particle luminescence, stacking faults, built-in electric fields, traps, microplasticity*

Mechanoluminescent (ML) materials convert the energy of mechanical deformation into optical emission. Thousands of compounds are reported to be capable of such behavior.[1−3] However, the vast majority require a significant threshold of input mechanical energy before emitted light is observed. Few examples of light emission under (quasi)reversible deformation are known. Among these compounds, manganese-doped ZnS (ZnS:Mn) has one of the lowest reported thresholds for ML appearance, in the range 0.53−0.6 MPa.[4,5] The extremely low threshold and the repeatable behavior of ML in ZnS:Mn make it a promising candidate for designing highly sensitive *in situ* nanometer-scale stress sensors for many applications in physical and biological systems.

The core tools of nanoscience, *i.e.*, nanoscale imaging and single-particle spectroscopies, combined with the tailored synthesis of precisely controlled nanostructures, have the potential to prove decisive in both understanding and controlling mechanoluminescence. In this work we will use nanoscopy tools to develop a set of observational algorithms for studying elastic mechanoluminescence. The resulting imaging and spectroscopic approaches can serve to guide future tailored synthesis of nanostructures that can act as efficient and reversible reporters of nanoscale forces in regimes of interest to biological scientists.

Received: October 24, 2020
Accepted: February 5, 2021
Published: February 17, 2021

https://dx.doi.org/10.1021/acsnano.0c08890
ACS Nano 2021, 15, 4115−4133

By the definition of mechanoluminescence, mechanical energy imparted to a solid is converted to light at luminescent centers. It is widely accepted[6−8] that, in the case of ML for II−VI semiconductors doped with Mn, photons are emitted from the $^4T_1$ − $^6A_1$ transitions of the Mn^{2+} ions, just as in photoluminescence (PL)[7] and electroluminescence (EL).[1,9] In contrast with PL,[7] the mechanism(s) of Mn^{2+} excitation in ML is still under debate. Different mechanisms have been proposed for the same material grown under different conditions (*e.g.*, if it was grown along different crystallographic directions or at different temperatures) or subjected to pressure in different matrices by rubbing, impact, fracturing, or compression.[1,4,5,10,11] In addition, typical ML samples are themselves quite heterogeneous, thus further complicating the interpretations of mechanism.

While we are particularly interested in investigating the mechanisms of (quasi-)elastic mechanoluminescence at low threshold deformations, it is important to first examine the hierarchy of mechanisms at different pressure ranges. These mechanisms are known from two independent lines of research, which offer alternative—and competing in the elastic regime of deformation—explanations for the origins of ML in ZnS:Mn. In this very brief survey, we will line up the mechanisms in order of decreasing excitation energy, starting from the best understood case of the highest energy plastic deformation ML and then progressively considering what happens as the energy of the mechanical deformation is reduced. We note that a full description of ML in all regimes requires an understanding of the processes running in both the mechanical (structural) and the electronic subsystems of the crystal and how these interact with each other in a variety of ways.

The high-energy, plastic deformation ML regime is observed at pressures above 10 MPa[12] in experiments using a quasi-static ramp of deformation. It is understood to involve irreversible glide of dislocations across the entire crystal.[13−17] The dislocations move freely and eventually arrive at a surface, resulting in a permanent change in crystal shape. In the next lower energy deformation regime, below ∼10 MPa, facile motion of dislocations is impeded by pinning points that are dispersed throughout the crystal. This transition region between the microplastic and elastic regimes is characterized by quasi- to fully reversible bowing of dislocation segments in between pinning points.[13,18] Hereafter, we will refer to the ML produced by dislocation bowing of both kinds (quasi- and fully reversible) as ML in the microplastic regime, while keeping in mind that such a process can extend to low deformations where completely elastic mechanisms may operate as well.[13]

In both the plastic and microplastic regimes, there is a similar overall coupling of the lattice motions to the electronic subsystem. It is widely recognized[19] that partial dislocations in ionic crystals of ZnS act as acceptors and carry large charge (0.65 e^-/site for ZnS:Mn[15]). When mechanical energy added to crystals by deformation exceeds the activation energy in the range between 0.46[16] and 1.16 eV,[20] one of the partial dislocations starts moving and interacting with electrons trapped at impurity levels within the screening radius of its electric field of ∼0.5 μm.[16] The resulting ionization of electrons is considered to be a two-stage process of thermal excitation to a certain level within the band gap, followed by tunneling to the conduction band.[21] These electrons can subsequently recombine with holes left in ionized Mn^{2+} impurities to produce deformation luminescence.

We turn now to lower energy deformations, where elastic phenomena may occur. The descriptions of ML in the elastic deformation regime come from a separate line of experiments, in which pressure was applied in transient pulses in the range 0.53−15 MPa.[1,4,5,8,10,22−24] In such experiments, ML pulses were shown to appear for more than 10 000 cycles,[5] invoking the development of an alternative ML mechanism based on the elastic piezo-phototronic effect, *i.e.* a three-way coupling among piezoelectric, semiconducting, and optical properties.[25] Proposed as early as 1962,[26] the mechanism as yet remains elusive. The currently most accepted model proposes the following: (1) onset of a strain-induced piezoelectric field $E_{\text{piezo}}\ [\text{V/cm}] = \frac{d_{33}\sigma}{\varepsilon_0(1+\chi)} = 3.8 \times 10^{-4}\sigma\ [\text{Pa}]$, where d_{33}= 3.2 pC/N is the piezoelectric coefficient, σ is applied stress, ε_0 = 8.85 pC/(V·m) is the permittivity of a vacuum, and $(1 + \chi)$ = 9.6 is the relative dielectric constant of ZnS; (2) piezoelectrically promoted detrapping of electrons from defect states to the conduction band of ZnS and subsequent (3) excitation of Mn^{2+} *via* nonradiative energy transfer.[5,7,10]

Importantly, however, any proposed mechanism for piezo-mechanoluminescence in ZnS:Mn must reconcile certain seemingly contradictory observations. On one hand, there is a dramatic increase in the observed ML intensity in the piezoelectrically active wurtzite structure of ZnS:Mn microparticles as compared to centrosymmetric, nonpiezoelectric zinc blende structures of the same material,[5] implying that phenomena related to piezoelectricity should be causal. The close resemblance of ML and EL spectra, kinetics, and intensity profiles also point to a piezoelectric connection.[4,26−28] On the other hand, there is a 1000-fold discrepancy between the threshold electric field of 10^6 V/cm = 62.5 mV/unit cell sufficient for EL excitation[29] and E_{piezo} = 330 V/cm = 0.02 meV/unit cell achievable due to the piezoelectric effect in the *pristine* wurtzite ZnS host at the typical ML threshold pressure of 1 MPa. This discrepancy is inconsistent with the simple piezo-phototronic mechanism, thus forcing a search for additional contributing factors.

In the present study, we develop an experimental approach to directly observe the occurrence of ML and its spatiotemporal patterns in single microparticles to the limit of optical resolution over a wide range of compressive forces. This approach contrasts with typical ensemble[5] and small-cluster[30] experiments, where observed outputs are averaged over a large number of, probably diverse, individual effects. Here, by observing individual ZnS:Mn particles under a series of pulsed deformations, we have been able to create a wide range of observables that we use to derive signatures associated with different mechanisms and build their hierarchy. We demonstrate that the mechanisms can operate simultaneously to different degrees across deformation regimes and, as excitation pressure increases, exist in a continuous transition from elastic to microplastic to plastic ML regimes. We provide evidence that below 8.1 MPa mechanoluminescence results from, sometimes simultaneous, operation of two independent mechanisms. One of these is dislocation-related mechanoluminescence in the microplastic regime.[13,17] Another one is an elastic piezo-phototronic mechanism. The latter mechanism dominates the mechanoluminescent output at this pressure range.

Once the hierarchy of the mechanisms is described, we proceed to the detailed investigation of the structural basis for the piezo-phototronic mechanism. For this purpose, individual

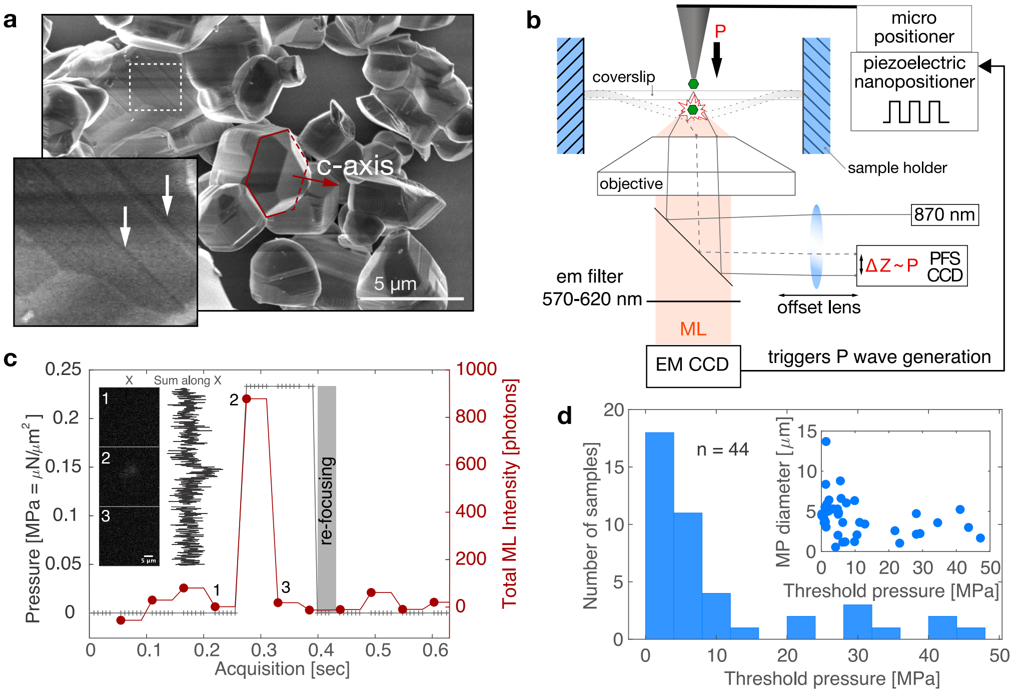

Figure 1. (a) SEM image of ZnS:Mn microparticles. The red line outlines the hexagonal shape of a single MP; the white rectangle outlines the region enlarged in the inset. Inset: White arrows show stacking faults (TEM characterization in Figure 5). (b) Experimental setup for real-time ML detection (see text; Methods). (c) Time-resolved mechanoluminescence of a single ZnS:Mn microparticle plotted along with an exciting pressure pulse. The MP diameter was 4.6 *µ*m; the MP was embedded in PDMS that covered the tip of the probe; ML images were collected with an exposure time of 50 ms (red circles indicate the start of every exposure cycle); pressure was detected every 8 ms (black bars); the range of ML registration wavelengths was λ_{reg} = 570−620 nm; strain rate was 0.125 *µ*m/ms; ML curve is shifted forward for 65 ms to correct for the time lag in detection of changes in pressure (see Note S1); inset shows 2D images of the ML intensity distributions at the three time points numbered in the main figure. (d) Distribution of threshold pressures for ML appearance for 44 single MPs at pressures ranging from 0.23 to 47.15 MPa. Inset: Threshold pressure plotted against MP diameter (the diameter is estimated from PL images of the particles).

particles are imaged separately by both high-resolution transmission electron microscopy and atomic force microscopy, so that the observables in mechanoluminescence can be directly traced back to the individual structural features within each particle. Overall, this advanced nanoscale structural characterization, conjoint with spatiotemporal dynamics of mechanoluminescence, points to a link between the piezo-phototronic mechanism and the long-known tendency of ZnS:Mn to produce multiple stacking faults with concomitant built-in electric fields. On the basis of these findings, we redefine the piezo-phototronic mechanism for low-threshold purely elastic mechanoluminescence in ZnS:Mn. Unlike previous models, our mechanism does not require the onset of large internal electric fields. Instead it relies on synergistic interaction between externally initiated piezoelectric polarization, internal electric fields, and trapped charges within the stacking faults of the ZnS:Mn crystal. By this synergy, the small piezoelectric polarization induced at low forces is amplified, thus allowing a small nondestructive elastic deformation to give a very bright ML signal, thereby explaining the apparent contradictions raised by previous models.

RESULTS AND DISCUSSION

Results are presented in three sections. In the first section, we describe the approach to direct observation of mechanoluminescence in single ZnS:Mn microparticles. The method provides a number of observables, including the magnitude, duration, and frequency of the pressure pulse, as well as the rate and pulse width of ML emission and the statistics of the distributions of the energy released in individual ML pulses. All of these observables are readily accessible for correlations with images of mechanoluminescence as well as of directly excited photoluminescence. We use the combinations of these parameters to distinguish the dislocation-related and the piezo-phototronic ML mechanisms in elastic, microplastic, and plastic regimes of deformation, even when they operate simultaneously. It is on this basis that we build the hierarchy of the mechanisms of mechanoluminescence. In the second section, we investigate the structural basis for the piezo-phototronic ML mechanism by nanoscale structural characterization of individual microparticles. In the third section, we provide experimental evidence that the presence of dislocations and stacking faults plays a vital role for the occurrence of mechanoluminescence in ZnS:Mn.

Real-Time Measurement of ML from Single ZnS:Mn Microparticles. ZnS:Mn microparticles (MPs) were synthesized *via* a solid state reaction under conditions optimized for the brightest ML.[5,31] Scanning electron microscopy (SEM) images of the resulting microparticles show highly faceted hexagonal shapes as expected for wurtzite crystals (Figure 1a). In accordance with SEM data, XRD analysis demonstrates the dominance of wurtzite (WZ) with 3% zinc blende (ZB) phase (see Figure S1). Importantly, most particles have multiple contrast variation bands perpendicular to its *c*-axis ([0001] direction), which can arise from stacking faults. One region

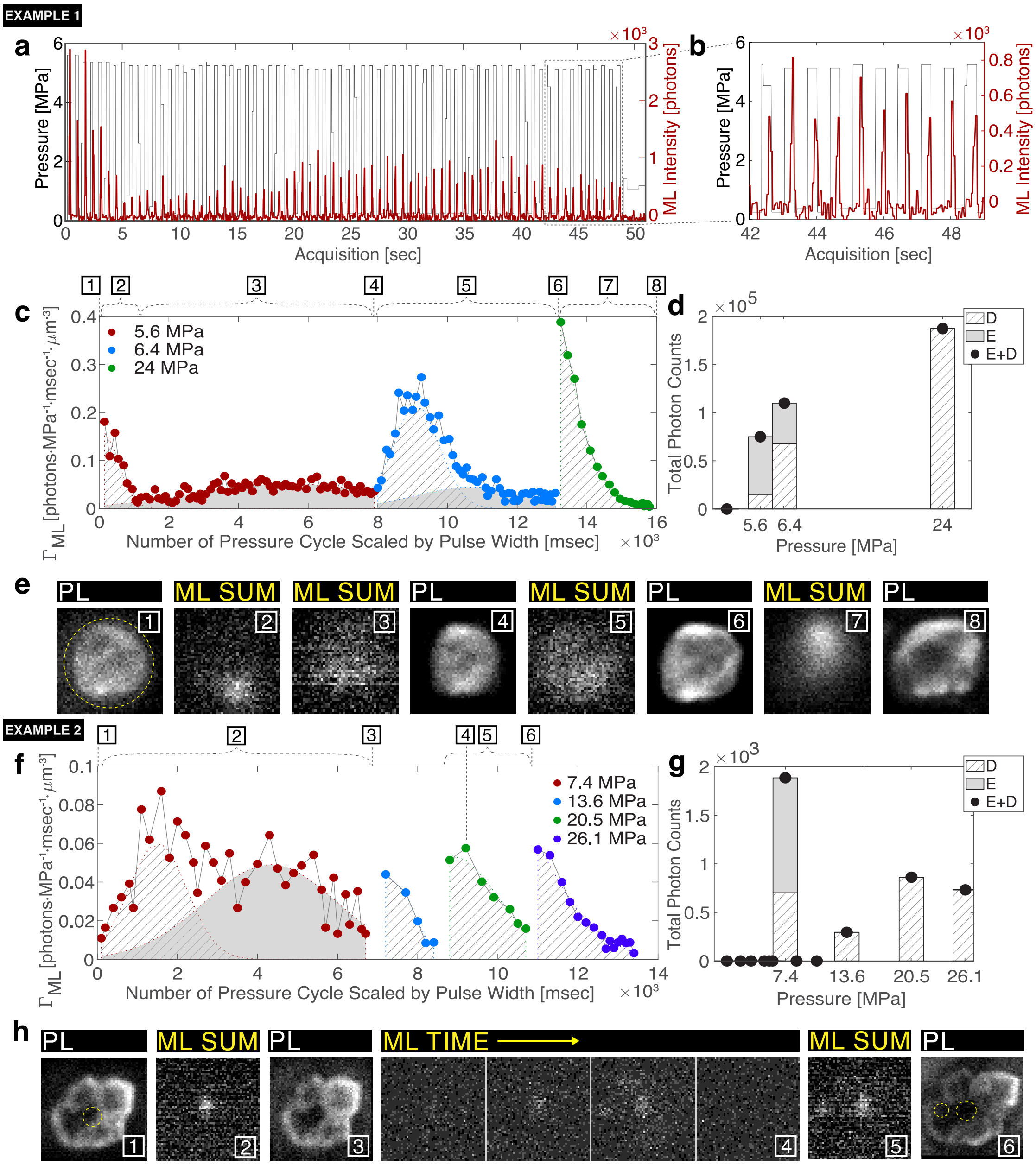

Figure 2. Examples 1 (a−e) and 2 (f−h) include data for two different single ZnS:Mn microparticles. (a) Time-resolved mechanoluminescence of a single MP excited by a cyclic compressive pressure of 5.6 MPa. Exposure time of ML registration was 50 ms; pressure was detected every 8 ms; the range of ML registration wavelengths was λ_{reg} = 570−620 nm, strain rate was 0.125 μm/ms; ML curve is shifted forward for 295 ms to correct for the time lag in the detection of changes in pressure (see Note S1). (b) Zoom-in on the last 10 ML pulses shown in (a). (c) ML emission rate Γ_{ML} calculated for each ML pulse within a series excited by a cyclic pressure of 5.6 MPa (red dots), 6.4 MPa (blue dots), and 24 MPa (green dots) and plotted *versus* the number of pressure cycles scaled by the pulse width *w*. Filled areas under each Γ_{ML} curve show fitted Gaussian functions corresponding to Pz- (solid filling) and μD−D-component (lined filling) of Γ_{ML}. (d) Total photon counts emitted by the MP within each series shown in (c) (black dots), also plotted separately for the Pz- (solid filling) and μD−D-component (lined filling) of Γ_{ML}. In addition, black dots are used to show the series with zero total photon counts. (e) 2D PL images of the MP for data shown in (c) taken before (1) and between pressure application series (4, 6, 8); sum projection of 2D ML images taken during the periods shown with curly brackets (2, 3, 5, 7); yellow circles show ML roi. (f) Same as (c) for different MP. Red, blue, green, and violet dots correspond to an excitation pressure of 7.4, 13.6, 20.5, and 26.1 MPa, respectively. (g) Same as (d) for data shown in (f). (h) Same as (e) for data shown in (f), along with the time-resolved distribution for the second peak of the third series (4).

exhibiting such features is highlighted with the white rectangle in Figure 1a.

Mechanoluminescence of single MPs was excited and recorded using a setup shown in Figure 1b (also see Methods, Note S1, and Figures S2 and S3). In contrast with previously reported single-particle ML studies,[32] this approach allows simultaneous detection of both imposed pressure and high-resolution 2D patterns of resulting ML. In this setup, the MP is embedded in PDMS or epoxy on the tip of a probe held by a micropositioner above a coverslip. The coverslip is mounted in an inverted wide-field microscope (Nikon Eclipse Ti2) equipped with a perfect focus system (PFS), which detects changes in the *z* position of the coverslip and automatically adjusts the position of the objective to maintain focus in real

Table 1. Fitting Parameters for Peaks Shown in Figure 2c and f[a]

		one-term Gaussian				two-term Gaussian						
		a_1	b_1	c_1	adj R^2	a_1	b_1	c_1	a_2	b_2	c_2	adj R^2
example 1	**5.4 MPa**	1176	7.5×10^{-7}	16.5	−0.0189	**4102**	**0.07**	**0.65**	**1230**	**5.37**	**3.77**	**0.8431**
	6.4 MPa	5791	9.2	1.236	0.8789	**5471**	**9.09**	**0.96**	**1127**	**10.64**	**2.24**	**0.9471**
	24 MPa	**1.74×10^5**	**19.27**	**1.79**	**0.9965**	0	14.27	0.17	1.74×10^5	19.27	1.78	0.9956
example 2	**7.4 MPa**	71.32	2894	3700	0.3625	**76.77**	**1512**	**1023**	**62.63**	**4327**	**2328**	**0.6269**
	15.6 MPa	**147.8**	**7300**	**766.2**	**0.9647**	312	8.07	5027	116.8	7385	559.1	NaN
	20.5 MPa	**226.7**	**8847**	**1613**	**0.9311**	−9725	9569	792.7	9903	9563	802.6	0.9734
	26.1 MPa	**281.8**	**9355**	**2234**	**0.9607**	-1.83×10^{18}	9473	247.1	5715×10^4	297.6	4503	0.9703

[a] **Bold** indicates statistically significant and physically reasonable fits chosen for determination of relative Pz- and μD−D-contributions.

time. Compressive force and resulting ML are generated by moving the microparticle toward the coverslip by a piezoelectric nanopositioner. Applied pressure causes deflection of the coverslip, which is detected by the PFS as a change in the depth of the focus, which is converted to pressure using the mechanical properties of the coverslip (Methods).

Operation of this system is illustrated for a single time-resolved ML flash excited by a rapid change in applied pressure (Figure 1c). In this example, pressure was applied for 150 ms and then released. The pressure pulse had a rectangular waveform with a strain rate of 0.125 μm/ms during application and release of pressure. Pressure was measured every 8 ms, whereas ML images were taken with an exposure time of 50 ms; that is, for every ML image there were six recordings of pressure. The ML pulse arrives at the moment of pressure application. Comparison of ML and pressure curves further reveals that the width of the ML pulse is 50 ms or less (as limited by the temporal resolution of ML detection) and is less than the width of the pressure pulse. The difference in the widths of the pressure and ML pulses can also be seen in 2D images of ML taken at time points right before, at the moment of, and immediately after the ML emission (inset to Figure 1c). We note that we do not observe any secondary ML peak at the moment of pressure release, as reported by other groups..[4,8,26,27] We relate this observation to the fact that pressure release is accompanied by refocusing, which requires 45 s at this pressure range, during which time ML cannot be detected (for details see Note S1 and Figures S2 and S3).

Application of the above single-pressure-pulse protocol to multiple individual particles revealed great heterogeneity in the threshold pressure for ML appearance. Forty-four MPs were subjected to pressure in the range of 0.23−47.15 ± 0.06 MPa, and the ML responses were recorded. As can be seen from Figure 1d, 100% of the particles emitted light within the tested range. Notably, some single ZnS:Mn MPs show an extreme sensitivity to mechanical stress. Twelve percent of the MPs emitted light at a pressure <1 MPa, with the lowest tested pressure being only 233 ± 60 kPa (Figure 1c). This level is lower than the minimum value of 600 kPa reported previously for an ensemble of ZnS:Mn microparticles sandwiched between two polymer films.[5] The data shown in Figure 1d also indicate that there is no size limit for the ML effect within the tested range of MP diameters (0.5−13 μm).

The threshold pressure varies between 0.23 and 47.15 MPa without a correlation with MP diameter (inset to Figure 1d). Furthermore, the total number of photons emitted per single ML pulse scales as a power of 0.56 ± 0.23 with increasing MP volume (Figure S5). This result is consistent with the idea that only part of the MP volume is involved in the ML process, with ML excitation being highly localized to specific internal structural features (further discussion below).

We also demonstrate that the observed ML does not arise from an interaction between the surface of the MP and the immediate environment. Bright ML was observed when a tungsten probe needle was substituted for steel, glass, or epoxy-covered probes as well as when the MP was immersed in water or physiological media (see Figure S6). The above observations confirm the conclusion that ML in ZnS:Mn is a fully endogenous physical process, which originates exclusively from internal properties of the material and does not require external triggers such as injection of carriers.

Identification of Three Different ML Mechanisms. When single ZnS:Mn MPs are subjected to cyclic loading, they emit repeatable pulses of light (Figure 2a,b). This behavior allows characterizing the dynamics of ML processes by experiments in which the same MP is subjected to multiple series of pressure cycles. Within each series, rectangular pressure pulses were imposed for 300−500 ms, each followed by an equal period of release. Pressure levels were measured every 8−20 ms, and ML images were collected with an exposure time of 50−100 ms. The amplitude of pressure remained the same within each series and was progressively increased in successive series. Detection of the first ML pulse defined the first pressure amplitude, which exceeded the individual ML threshold of the MP under test. We then ran the series at the same pressure amplitude until ML emission stopped, presumably due to exhaustion of the trapped carriers with given activation energy (see the introductory section). The amplitude of the pressure was then increased until ML emission reappeared, and a second series of cycles was imposed at that pressure. This process was repeated until finally, after, in total, 21−141 ML pulses, further increase in excitation pressure did not produce any light (see more details on factors affecting the total number of ML pulses in Note S2). Note that some pressure increments did not produce light. These increments are omitted in Figure 2c,f and are shown by black dots at zero level in Figure 2d,g.

To be able to compare the ML outputs from different MPs at different pressure amplitudes, we calculated the ML emission rates:

$$\Gamma_{\mathrm{ML}} = \frac{I_{\mathrm{total}}}{\sigma w_{\mathrm{ML}} V}$$

where $I_{\mathrm{total}}(x, y, t) = \int_{w_{\mathrm{ML}}} \int_{\mathrm{MLroi}} I_{\mathrm{px}}$, $I_{\mathrm{px}} > I_{\mathrm{th}}$ is the pixel intensity in photons, I_{th} is threshold pixel intensity used for the whole series excited by pressure of a given amplitude, ML roi is determined manually from the sum projection of all frames of the ML stack, w_{ML} is the pulse width in ms, σ is the applied

https://dx.doi.org/10.1021/acsnano.0c08890
ACS Nano 2021, 15, 4115−4133

Scheme 1. ML mechanisms operating at different pressure ranges with corresponding properties defined in the text; Γ_{ML} is the ML emission rate, w_{ML} is the width of the ML pulse, w_P is the width of the pressure pulse; *provisional limit of the microplastic regime defined by the lowest pressure at which μD-component is observed in our experiments.

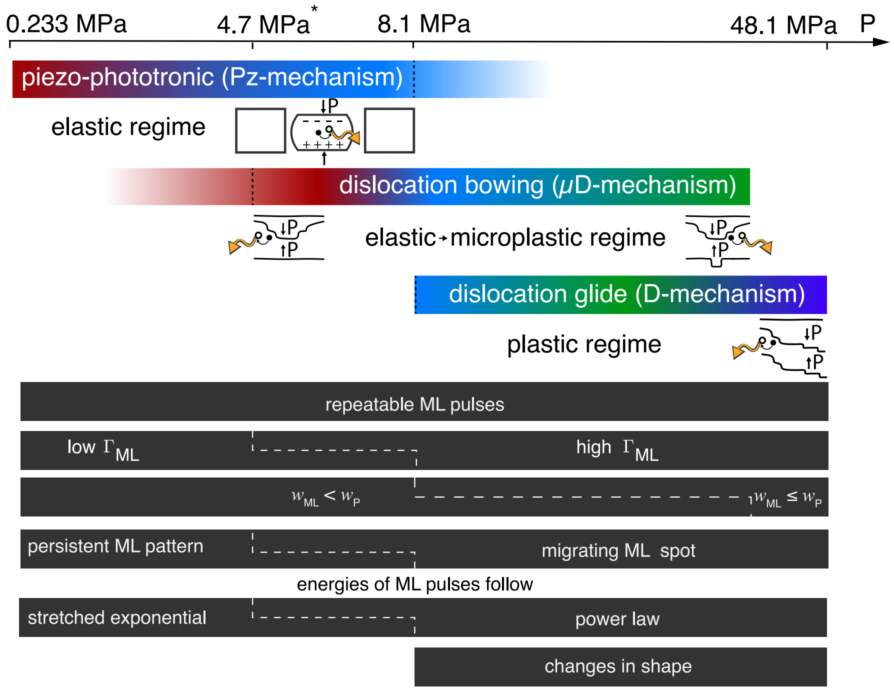

pressure measured in MPa, and $V = \frac{4}{3}\pi r^3$ is the ML-emitting volume in μm^3, where r is the radius of the ML roi.

Figure 2c,f show Γ_{ML} for two different representative MPs excited by pressures ranging from 5.6 to 26.1 MPa (additional examples and time-resolved ML and pressure plots for all series can be found in Figures S7−S9). At pressures below 8.1 MPa, Γ_{ML} curves encompass components with significantly different maximum ML emission rates. The presence of two different components with higher and lower Γ_{ML} is especially clear in Figure 2c in the series of ML pulses excited by the pressure of 5.6 MPa (red dots).

These two components can be separated by fitting Gaussian functions. The number of Gaussian functions (one or two) fitted to the curve for a given pressure amplitude is decided based on the best fit parameters and corresponding R^2 values (Table 1). Then, calculation of the areas under the fitted curves in Figure 2c,f provides the relative contribution of the two components to the total ML output (Figure 2d,g). It can be seen that the component with lower Γ_{ML} (solid filling) appears only at pressures below 8.1 MPa. Furthermore, in the first series in both examples, this component dominates the total photon counts, whereas the component with higher Γ_{ML} (hatched filling) dominates early in the same series but is exhausted faster, ultimately producing a smaller fraction of light. In contrast, ML emission at pressures above 8.1 MPa is completely due to the component with higher Γ_{ML}.

The distinct responses of the components to increasing pressure suggest that different mechanisms dominate the production of ML in low- and high-pressure regimes. Taking into consideration that the component with lower Γ_{ML} produces most of the light at lower pressures and disappears at pressures above 8.1 MPa, it seems reasonable to assume that this component is due to the elastic piezo-phototronic mechanism (hereafter the "Pz-component").[5,10] The component with higher Γ_{ML} can then be ascribed to deformation ML (hereafter the "D-component").[13−15] By this interpretation, both mechanisms, piezo-phototronic and deformation-related, operate at pressures below 8.1 MPa. Moreover, they operate simultaneously at the beginning of the pressure series as arises from the overlapping Gaussian fits. In contrast, above the 8.1 MPa limit, the deformation ML is the only mechanism in our experimental protocol.

As discussed in the introductory section, production of ML by the piezo-phototronic mechanism (Pz-mechanism) is strictly elastic,[10] whereas deformation-related mechanisms can be either plastic (D-mechanism), if dislocations gain enough energy to unpin and glide irreversibly,[17,18] or microplastic-elastic (μD-mechanism), when governed by quasi- to fully reversible dislocation bowing at lower pressures. These descriptions use the term "elastic" in a strictly mechanical sense; that is, we assume that an elastic ML process does not lead to any structural changes persisting after pressure is removed. At the same time, with respect to the electronic structure of the material, detrapping of carriers to produce ML is irreversible, as there is no source to refill the traps. Thus, despite the elastic nature of the deformation, the process is not entirely reversible.

Following the above definitions, we conclude that elastic, microplastic, and plastic regimes of ML excitation exist as a partially overlapping continuum with only nominal limits (Scheme 1). The mechanisms of any type in any combination can potentially operate at any of these regimes. The key point is in such a mixed operational mode the piezo-phototronic and dislocation-related mechanisms have different structural bases and, thus, can consume distinct sets of trapped carriers. Overlaps can occur, *e.g.*, when the elastic Pz- and microplastic μD-mechanisms operate simultaneously as at the threshold pressures in examples shown in Figure 2 (red dots). We also present evidence that these two types of ML are produced at spatially distinct luminescent centers (the next section) and describe a structural basis of the Pz-ML (see Discussion). Another example is simultaneous operation of the Pz- and D-mechanisms when the pressure, sufficient to initiate plastic deformation, is applied to a previously untreated particle in the first series. In this case, however, the structures producing ML by the Pz-mechanism are likely to be quickly destroyed by plastic deformation as implied by an absence of the component with lower Γ_{ML} (see Figure S10).

Current data provide rough estimates for some of operational ranges for different ML mechanisms. Based on appearance of ML at 0.233 MPa (Figure 1c), we set the lower limit for the Pz-mechanism at this pressure value, whereas its higher limit is not defined in our experiments. In our experimental protocol, we relate the disappearance of the Pz-component at pressures above 8.1 MPa (Figure 2) to the fact that we ran the pressure cycles until a given excitation energy stopped producing ML (above). The actual higher limit of the Pz-mechanism may be at higher pressures, at which the structural basis of the Pz-ML is destroyed by plastic deformation (see Discussion). Also, we use 4.7 MPa, the lowest pressure, at which we observe the component with higher Γ_{ML} (Figure S9), to set a provisional limit for the onset of μD-process. A pressure of 8.1 MPa can serve as the lower limit for the plastic D-mechanism because we begin to observe the permanent changes in particle's shape only above this pressure (see the next section).

The three mechanisms are further defined and distinguished by the spatiotemporal dynamics of PL and ML patterns and energy output distributions as described below. Unique combinations of these observables serve as signatures for each of three mechanisms and are summarized in Scheme 1. In some situations, where the distinction between μD- and D-mechanisms is impossible, we refer to ML excited by dislocation motion of any type as arising from a μD–D-mechanism.

The Pz-, μD-, and D-Mechanisms Are Distinguishable by Their PL and ML Spatiotemporal Dynamics. PL images of the MPs reflect their shapes and thus can be used to indirectly evaluate the relative extent of plastic deformation in Pz- and μD–D-dominated pressure series. By definition, elastic ML as seen at low pressure is not accompanied by structural alterations. At the other extreme, at high pressure, ML emission during plastic deformation is accompanied by irreversible changes in shape and structure.[13,14] Correspondingly, in both examples analyzed above (Figure 2), the shape of the MP as defined by PL images was not visibly altered in the lowest pressure series, *i.e.*, after 40 pressure cycles at 7.4 MPa (compare Figure 2h (1) and (3)) and 72 cycles at 5.6 MPa (compare Figure 2e (1) and (4)). This result is consistent with predominantly elastic behavior of both observed components, Pz and μD. In the latter case, the potentially produced microplastic changes may be too small to be resolved by optical microscopy. In contrast, the shape of the MP was dramatically altered by application of higher pressures in series with only the μD–D-component, *e.g.*, Figure 2e (6, 8) and Figure 2h (3, 6), thus directly confirming the plastic nature of this regime and its basis in deformation ML.

The three ML mechanisms can also be differentiated by several features of ML spatiotemporal dynamics. However, there is an important exception: at all examined pressures, and thus throughout all three regimes (P, μD, and D), we observed repeatable ML pulses as excited by repeated imposition of pressure of the same amplitude (Figures 2 and S9). For ML by the Pz- and μD-mechanisms, such behavior is not unexpected, as in these cases the ML process is considered to be driven by a nondestructive piezo-phototronic effect and (quasi)reversible dislocation bowing, respectively (Scheme 1).

However, we also observe repeatable ML pulses at high pressures where PL images document the occurrence of irreversible changes due to the D-mechanism. This is a rather unexpected phenomenon. Previous work[16] has established that, during plastic deformation, unpinned dislocations sweep through the volume of the material, emptying filled traps along the way, and dissipating at the surface. However, this picture has emerged from studies in which deformation ML was observed throughout the course of continuously increasing deformation, and, once deformation was stopped, resumption of light required the application of higher pressure.[13−15] In the present study, ML was excited by a train of short pressure pulses. In this protocol, repeated ML pulses in the plastic regime can be understood in terms of the Peierls mechanism and abrupt kink model of dislocation motion.[19,33] According to this model, a kink pair is first formed on a straight dislocation and then these kinks migrate along the dislocation line, overcoming the periodical Peierls potential in the direction of motion. The reappearance of light in successive pressure cycles implies that, in each cycle, the kink stops at the moment of pressure release or ML cessation, whichever occurs sooner, and that the duration of the single ML pulse is insufficient for the kink to reach the surface and dissipate. Then, in the next cycle, kink migration continues and ML again appears.

Although the repeatability of pulses does not distinguish the D-mechanism from the P- and μD-mechanisms, this distinction can be made by considering the widths of ML pulses w_{ML} (Figure S11). In particular, in the Pz-dominated series, w_{ML} was always less than the width of pressure pulses w_P and remained within the range of $(0.15-0.6)w_P$. In contrast, the typical picture within μD–D-series is progressively decreasing w_{ML}, from $w_{ML} = w_P$ at the first cycle to $0.2w_P$ at the last cycle. We speculate that, for the Pz-mechanism, w_{ML} is less than w_P due to self-compensation, which arises in the semiconductor in response to the pressure-generated piezoelectric field (more details in Discussion). In the μD–D-series, we can understand the decreasing w_{ML} as reflecting impeded and unimpeded motion of dislocations. During both (quasi)-reversible bowing and irreversible glide, dislocation can meet some structural or electrical obstacles with an unpinning energy that is higher than the ML activation energy and therefore stop prior to the release of pressure resulting in $w_{ML} < w_P$. Only when dislocations are unpinned (the D-mechanism) and do not meet high-energy obstacles does $w_{ML} = w_P$. Thus, $w_{ML} = w_P$ provides a strong indication for a plastic process.

Finally, ML spatial patterns also help to distinguish the mechanisms. For this purpose, 2D ML images were summed along the time axis for all or part of a pressure series in which one or the other regime dominates ("ML sum" in Figure 2e,h) or, alternatively, were examined over time during a single ML pulse ("ML time" in Figure 2h, also Movies S1–S4). ML pulses produced by the Pz-mechanism are emitted from the same spatial area at each time within a pressure series and, then, from one pressure series to the next (Figure 2e (3) *vs* (5) and Figure 2h (2); time series are provided in Movie S1). This observation is in agreement with prediction because the ML-emitting structure is not altered in the elastic regime. In

Table 2. Best Fit Parameters for the Distributions of Energy in the ML Pulse Series Shown in Figure 2c Fitted to the Power Law and Stretched Exponential Distributions Defined in Table S1[a]

	power law			stretched exponential			log-likelihood ratio test		
	$p(x) = Cx^{-\alpha}$			$p(x) = Cx^{\beta-1}e^{-\lambda x^{\beta}}$					
data set	α	$b_{\min}$	p-value	λ_{est}	β_{est}	p-value	λ_{LR}	p-value	support for power law
5.6 MPa {Pz, μD−D}	1.42	27.00	0.00	0.02	0.70	0.00	−3.29	**0.00**	none
5.6 MPa Pz	1.46	27	0.07	0.1×10^{-3}	1.59	**0.99**	−5.57	**0.00**	none
{5.6 MPa, 24 MPa}μD−D	1.29	200	**0.99**	0.34	0.18	**0.99**	−1.36	0.17	moderate

[a] $b_{\min}$ denotes the lower bound of the fits; λ_{LR} is the log-likelihood ratio for the power law tested against the stretched exponential, positive log-likelihood ratios indicate that the distribution is favored over the alternative;[38] the last column presents our judgment of the statistical support for the power law hypothesis against the stretched exponential; "none" indicates data sets that are probably not power-law distributed; "moderate" indicates that the power law is a good fit but an alternative remains plausible; statistically significant p-values are given in **bold**.[38]

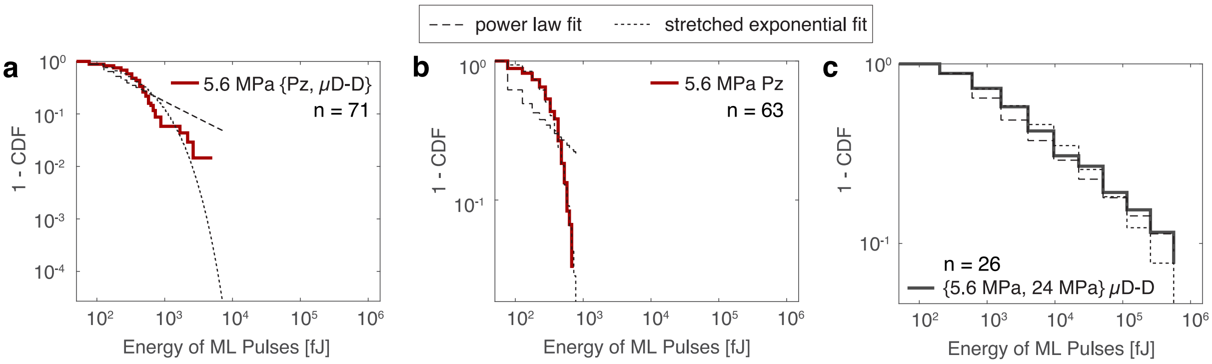

Figure 3. Empirical distributions (as complementary cumulative density functions (CDFs)) of energy in the ML pulse series shown in Figure 2c excited by a cyclic compressive pressure of 5.6 MPa (a−c) and 24 MPa (c), along with the best fitting power-law distribution (dashed line) and stretched-exponential distribution (dotted line); (a) includes all data points for the excitation pressure of 5.6 MPa, whereas (b) shows only the last 63 data points (Pz-component) of the 5.6 MPa data set; (c) represents the distributions for combined μD−D-components for the excitation pressure of 5.6 MPa (the first eight data points) and 24 MPa (all data points).

contrast, series dominated by the μD−D-mechanism(s) are characterized by the ML spot with changing location or pattern, both between and/or within pressure series. For example, the ML spot shown in Figure 2e migrates from the location in (2) to the location in (7) over the course of three pressure series, likely following the glide of dislocations (Movie S2). An additional example of μD-D-ML for another microparticle is provided in Movie S3. And in Figure 2h (4), time-resolved 2D images of a single ML pulse show that the ML emitting area is spreading from the center out to the edges of the MP. This pattern repeats in each pressure cycle and arises in the same spatial area of the particle (Movie S4) as opposed to a migrating ML spot seen in Figure 2e (2, 7). This type of pattern matches that expected for quasi-elastic dislocation bowing.

The Energies of ML Pulses Produced by Pz- and μD−D-Mechanisms Follow Different Statistical Distributions. To further explore our conclusion that ML emerges from both an elastic Pz-component and a deformation ML component (by consolidated μD−D-mechanisms), we tested the hypothesis that the Pz-component exhibits Gaussian-like dynamics, as required to describe a multiplicative stochastic process, *e.g.*, a stretched exponential or log-normal distribution, whereas the μD−D-component follows a power law. The rationale for these predictions is as follows. As revealed by acoustic emission experiments in hexagonal close packed (hcp) crystals, the distributions of acoustic energies released by discrete plastic events are independent of the nature of atomic bonds and the type of defects and represent a well-established case of a power law implying that the process is scale-free with the same proportion of events with higher and lower energy.[18,34,35] Moreover, power-law dynamics is argued to appear at every applied stress including that lower than dislocation unpinning stress.[36] Since ML pulses by the μD−D-mechanisms (Scheme 1) are the other form of energy released by dislocation motion, they can be expected to follow a power law as well.

In consequence, in hcp crystals, Gaussian-like, non-power-law ML dynamics can be taken as excluding μD−D-mechanisms. If so, it can be expected for the piezo-phototronic ML, in which case strain defines the amplitude of the piezoelectric field and thus sets the energy scale. A Gaussian distribution offers a classic description for such a process. However, as Pz- and μD-mechanisms often operate simultaneously (Figure 2 and Scheme 1), there is a possibility of events of a mixed type with the amplitude larger than the one expected from a Gaussian distribution. Thus, heavy-tailed distributions, such as a stretched exponential or log-normal, appear to be the most plausible description for the distribution of energies released by the piezo-phototronic process. A stretched exponential is particularly useful in the present case as, by varying its parameter β from $\beta = 2$ to $\beta \to 0$, it is possible to interpolate between Gaussian and power law distributions, respectively.[37]

Our hypothesis was tested using the method previously described in ref 38. This approach includes maximum-likelihood fitting, determination of goodness of fit based on the Kolmogorov—Smirnov test, and log-likelihood ratio tests

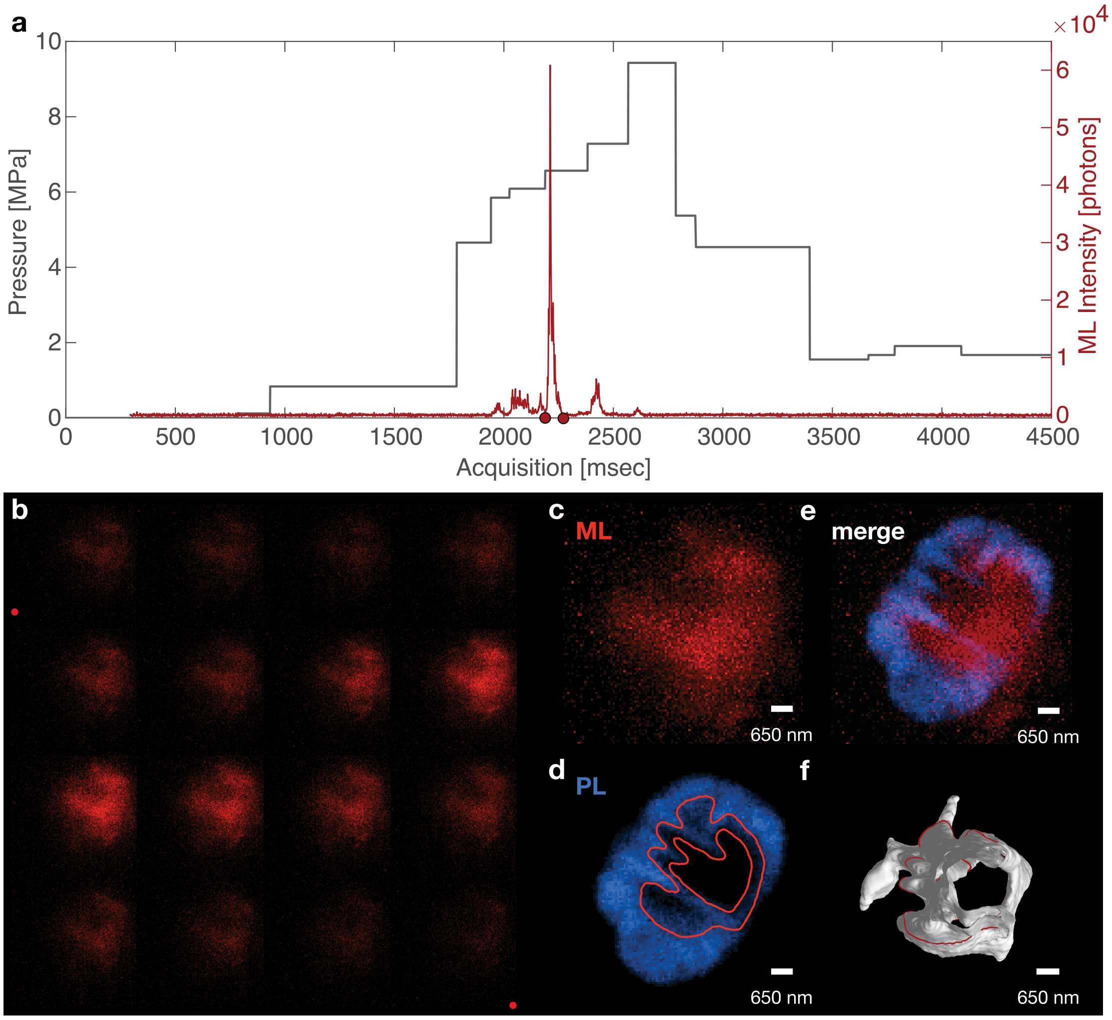

Figure 4. (a) Time-resolved mechanoluminescence of a single MP excited by a single pulse of pressure. Exposure time of ML registration and temporal resolution of pressure detection were 0.633 ms; red dots mark the first and the last frames of the ML pulse shown in (b). (b) Time-lapse images of the ML peak revealing striations. (c) Sum projection of all frames for the ML flash shown in (b). (d) PL image of the particle from (b) and (c) taken at the plane of ML registration. Red lines outline outer and inner grain boundaries inside the particle as revealed by thresholding the PL image of the particle (12.55% at the middle range of intensity). (e) Merged ML (red) and middle plane PL (blue) images of the particle from (b)−(d) showing that stripes in ML and PL patterns do not overlap. (f) 3D isosurface representation of the grain boundary (one plane shown in (d). The outer luminescent layer is removed for clarity; red contour line highlights the MP *z*-plane shown in panels (b)−(e). PL images are taken with the excitation wavelength λ_{ex} = 365 nm. The registration wavelength λ_{reg}= 570−620 nm is the same for both ML and PL registration.

for comparing the experimental distribution against competing theoretical distributions (more details can be found in Methods). The energy of a single ML pulse was calculated as $E_i = E_{\mathrm{ph}} I_{\mathrm{total}\,i}{}^{2}$, where $E_{\mathrm{ph}} = 3.34 \times 10^{-4}$ fJ is the energy of a photon of 595 nm light. Tests were run for every series in Figure 2c, separately for μD−D- and Pz-components of the 5.6 MPa series (the first 8 and the last 63 data points, respectively), and for a combined μD−D-data set comprising the first 8 data points of the 5.6 MPa series plus all data points of the 24 MPa series. Also we analyzed the data set including all data points from all series in Figure 2c. Best fit parameters along with *p*-values for goodness of fit for all tested theoretical distributions, all binning schemes, and all data sets are shown in Table S2 and Figures S12 and S13. Statistics for example 2 shown in Figure 2f is similar to example 1, so we do not discuss it in detail. Results of statistical tests for example 2 are given in Tables S4 and S5 and Figures S14 and S15.

In the first series in Figure 2c, where μD−D- and Pz-components are well resolved, it is possible to analyze the Pz-component separately. Among five tested distributions, the power law is ruled out (p_{pl} = 0.00) and only fitting to the stretched exponential and log-normal distributions returns statistically significant *p*-values, $p_{\mathrm{st-exp}}$ = 0.99 and $p_{\mathrm{lg-norm}}$ = 0.91 (see Tables 2 and S2). The likelihood ratio test excludes the log-normal distribution as well (Tables 2 and S3). Hence, the stretched exponential is strongly supported: it is both a good fit to the data and a better fit than the alternatives. Importantly, running the test for all data points of the 5.6 MPa series (and thus the combination of μD−D- and Pz-components) does not support any distribution (Tables 2, S2, and S3). Figure 3a and b show the full 5.6 MPa data set and its Pz-component along with the best fitting power law and stretched exponential curves. It can be seen clearly that the empirical curve for the full 5.6 MPa data set includes two

https://dx.doi.org/10.1021/acsnano.0c08890
ACS Nano 2021, 15, 4115−4133

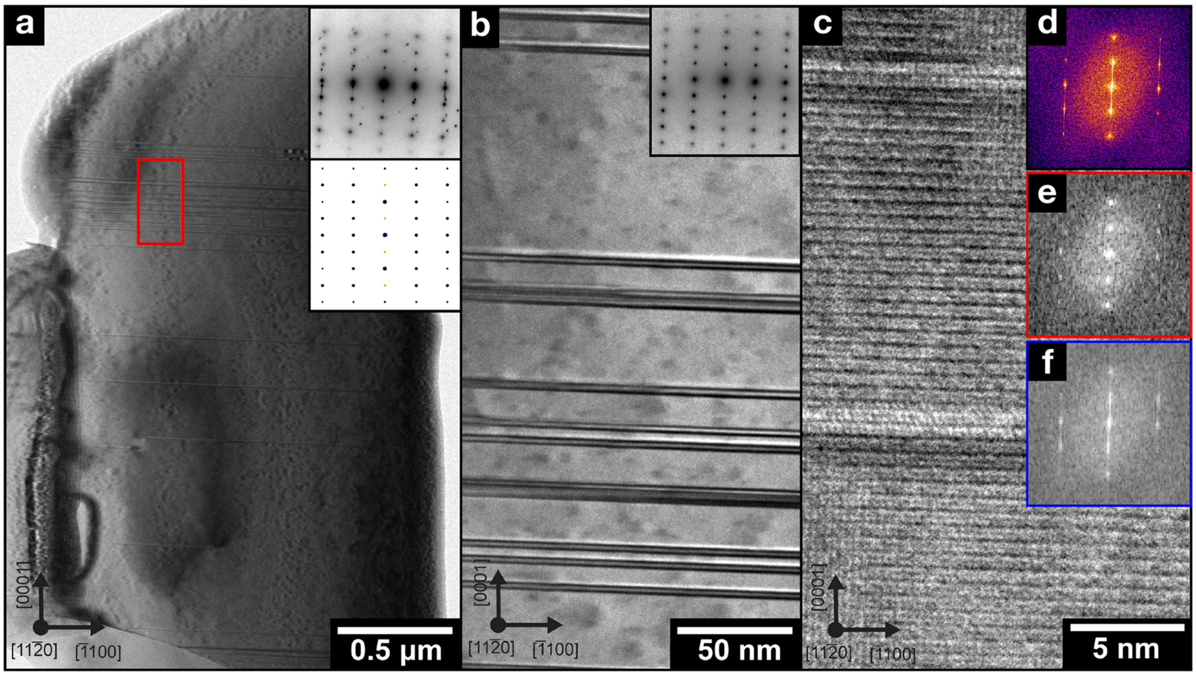

Figure 5. (a) Bright field TEM image of an FIB lamella of a ZnS:Mn microparticle (not the same one imaged optically) viewed down the [11$\bar{2}$0] zone axis with an inset electron diffraction pattern (top) and simulated diffraction pattern (bottom). (b) Zoomed-in bright field TEM image from the upper part of the particle roughly from the region in the red box in (a) with inset electron diffraction pattern. (c) High-resolution TEM image of the stacking disorder with (d) an FFT from the whole image (we note all FFTs were carefully processed with a Hanning window to avoid image edge artifacts), (e) a pristine wurtzite region, and (f) a faulted region. In total, the particle has a basal plane stacking fault density of ∼11 stacking faults per micron along the *c*-axis. However, this distribution is not uniform, and in the highly faulted areas, the density can be as high as 40 faults/μm.

components with distinct behavior, as also inferred from all of the evidence presented above.

For analysis of distributions from the μD−D-component series, we combined the 8 data points of the μD−D-component portion of the 5.6 MPa series with all data points of the 24 MPa data set, which is also exclusively ascribed to the μD−D-component based on a goodness of Gaussian fits (Table 1). The resulting μD−D-data set is fitted well to the power law, stretched exponential, and log-normal (see Figure 2c, Tables 2 and S2). On the basis of the result for the Pz-component of the 5.6 MPa series, we can exclude the log-normal distribution from consideration. However, the remaining power law and stretched exponential cannot be distinguished, as the likelihood ratio test is inconclusive (Tables 2 and S3). So both distributions receive moderate support. It is not surprising as the sample size is naturally low and the β parameter of the stretched exponential is 0.18. The latter is in accord with previously mentioned convergence of the stretched exponential toward the power law with decreasing β.[39] Comparison of β parameters for the Pz-component of the 5.6 MPa series and combined μD−D-data set (1.7 *vs* 0.18) shows that such convergence does occur, thus strengthening the power law case for the μD−D-data set. Importantly, the power law holds for almost all data bins with the lower bound $b_{\min}$ fixed at b_2.

The 20.5 MPa series shown in Figures 2f and h (4,5) support the existence of the scale-free behavior in the microplastic region predicted in ref 36. From Figure 2h (4) and Movie S4, it can be seen that dislocations bow rather than glide throughout the whole pressure series (as judged from the repeatable pattern of light spreading from the center out to the sides of the MP in each pressure cycle). At the same time, the best fit parameter $\beta = 0.94 < 1$ of the stretched exponential ($p = 0.99$), high goodness of power law fit ($p = 0.99$), and failure of the likelihood ratio test to distinguish between the power law and stretched exponential (Tables S4 and S5) imply that the system is in a state of criticality.

Best fit $\beta \approx 2$ for the Pz-components for both examples in Figure 2 (1.7 and 1.5 for examples 1 and 2, respectively; Tables 2, S2, and S4). This is indicative of Gaussian-like dynamics.[37] Hence, these values can be taken to entertain the possibility that operation of the system in the Pz-dominated series remains preliminarily elastic and that arbitrary distinction of the μD−D- and Pz-components, based on the shape of the Γ_{ML} curves and disappearance of the Pz-component at higher pressure, can be correct.

ML Photons Produced by the Pz-Mechanism Form Persistent Spatial Patterns. The predominantly elastic nature of ML excited by the pressures below 8.1 MPa is strongly supported by the above analysis. The characteristic feature of this regime is that light is emitted in persistent spatial patterns (Figure 2) from a subvolume within the particle (Figure S5). At the same time, according to the current model of elastic ML, a strain-induced piezoelectric field serves as the energy source for Mn^{2+} excitation.[5,10,23] This model considers pristine wurtzite ZnS, in which case a piezoelectric field is established in the whole volume of compressed MP. In consequence, resulting ML is predicted to emanate from the whole volume as well. This expectation is in contradiction with our observations.

To investigate this issue further, we recorded ML excited by a single pulse of pressure with a high temporal resolution of 633 μs (Figure 4a). Light first appeared at 5.8 MPa, with the majority of ML output generated by the pressure of 6.6 MPa. A

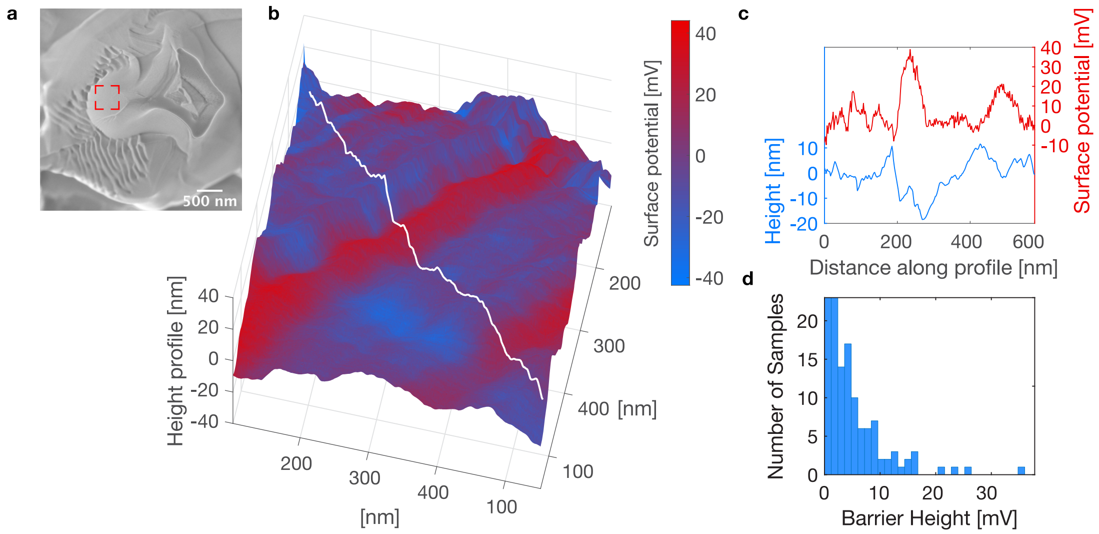

Figure 6. (a) SEM image of the MP after FIB treatment. Red dashed rectangular shows one of the areas scanned by AFM. (b) AFM image of the microparticle interior exposed by FIB treatment. Topology is shown as a 3D profile, which is color-coded to visualize the KPFM potential. (c) Profiles of height (blue) and KPFM potential (red) along the white line shown in (b). (d) Distribution of potential barrier height calculated from KPFM potential data for different areas of the sample.

striking feature of the ML image series is the stripes persisting over the whole ML flash (Figure 4b and c, Movie S5). When the ML pattern is overlapped with the PL image taken at the same *z*-plane before pressure application (Figure 4c−e), it can be clearly seen that ML photons are emitted from the central part of the MP and that the ML striation does not overlap with the features seen in the Mn^{2+} PL map. Analysis of the 3D PL image (Figure 4d and Figure S16) further reveals an inhomogeneous internal structure spreading across the whole MP volume. This pattern implies that either certain 3D structures inside the particle contain fewer Mn^{2+} ions or, as seems more likely, the PL efficiency of Mn^{2+} ions located within these internal structures is lower than in the outer part of the MP. As shown in Figure 4f, thresholding the PL intensity unveils an isosurface that separates the PL bright and dark regions within the particle. Mn^{2+} PL intensities outside of this shape are higher than those inside of it. The red contour lines in Figure 4d,f highlight the *z*-plane shown in Figure 4d, revealing that the PL isosurface roughly resembles the features of the ML pattern. Thus, ML photons emanate from the dark PL region, a structure of microscopic size that spreads across the central part of the MP and is aligned along its *c*-axis. More details on the role of Mn doping in the ML process are given in Note S3 and accompanying Figures S16−S20.

Structural Basis of the Pz-Mechanism: Stacking Faults and Concomitant Electric Fields in ZnS:Mn MPs. ZnS is well known for its polytypism[40] and has a strong tendency to produce stacking faults, which are accompanied by strong built-in electric fields.[41] Such effects could explain the spatial heterogeneity of the ML (Figure 4), as well as ML emission from a subvolume of the MPs (Figure 2e,h and Figure S5). If so, they would be likely candidates to underlie persistent spatial ML patterns produced by the Pz-mechanism.

To confirm the presence of stacking faults, we used the focused ion beam (FIB) lift-out (LO) technique to prepare a cross-sectional transmission electron microscopy (TEM) specimen of a ZnS:Mn MP (see Methods). Figure 5a shows a bright field TEM image of the FIB slice of a whole microparticle viewed down the [11$\bar{2}$0] zone axis with an inset electron diffraction pattern and simulated electron diffraction pattern for the wurtzite [11$\bar{2}$0] zone axis. Faint stripes can be observed, which are consistent with basal plane stacking faults and zinc blende inclusions. Figure 5b shows a magnified view from the top part of the particle highlighting the basal plane stacking disorder present in the sample. A high-resolution TEM (HRTEM) image shown in Figure 5c includes two zinc blende inclusions, each of which are ∼2 nm long. A wider field of view HRTEM image is shown in Figure S21. Fast Fourier transform (FFT) of the entire image is shown in Figure 5d. Streaks of FFT spots are indicative of stacking disorder. Further we show an FFT from a pristine wurtzite region in Figure 5e with no apparent streaks and from the faulted region in Figure 5f, which has obvious streaks. If we view the sample down the [1$\bar{1}$00] zone axis (Figure S22) the stacking fault contrast disappears, confirming all the observed defects are stacking faults and zinc blende inclusions. Based on the TEM data presented here, we can confidently conclude that there is considerable, well-defined but nonuniform, stacking disorder in the microparticles.

Coexistence of alternating hexagonal and cubic crystal phases can lead to the appearance of built-in electric fields due to the interplay of spontaneous polarization in the hexagonal phase, the band gap offset between ZB and WZ domains, and quantum confinement effects.[40,42,43] This type of heterocrystalline structure naturally occurs in SiC[44−46] and ZnS.[41,47] It also has been introduced synthetically in 1D III−V nanowires[48−50] and ZnCdS microparticles.[51,52] ZnS has a greater tendency to produce stacking faults compared to other II−VI semiconductors.[53] This is a consequence of a distinctive combination of very low (4−6 meV/atom[54−57]) difference in total energy between the hexagonal (2H) and cubic (3C) phases and the relatively low ionicity of the crystal lattice.[58] The balance is very delicate, and CdS, which is isostructural to ZnS but has a slightly higher 2H/3C energy difference[54] and more ionic crystal lattice,[58] shows very little or no polytypism. Moreover, the hexagonality of ZnCdS and ZnMnS solid solutions rapidly increases with increasing amount of Cd, Mn, and other dopants,[59,60] leading to the disappearance of

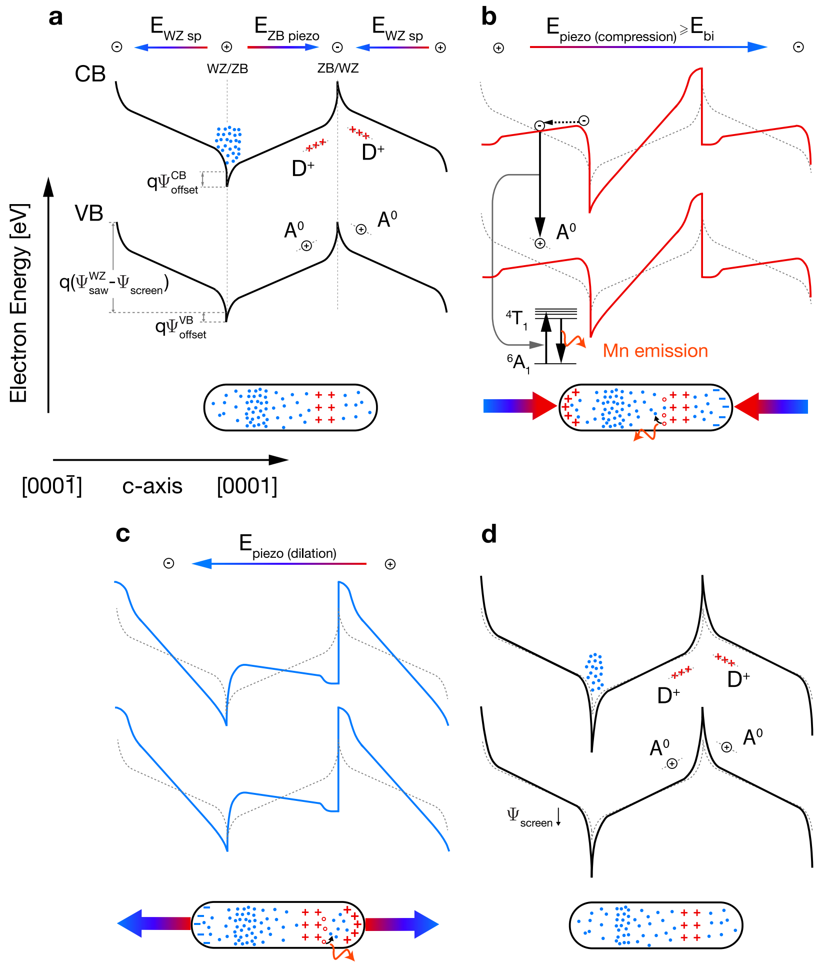

Figure 7. Energy band diagram illustrating the model of mechanically induced mechanoluminescence in faulted ZnS:Mn. Panels represent a WZ/ZB/WZ sequence that comprises the structural unit of the model (a) in the absence of external stress, (b) compressed, (c) dilated, and (d) after multiple emission cycles. Red pluses and blue minuses represent polarization charges created by electric fields and localized states. Free electrons and holes are shown by blue and empty red circles, respectively. For the WZ phase, we show 2H modification with maximum hexagonality; however, a distribution of 6H, 4H, and 2H modifications can exist in the crystals.[41] The ZB phase has only 3C modification, with the 2H/3C interface producing the highest potential barrier. Gray dotted lines in panels (b)−(d) show bands before pressure application. Other notations are defined in the text.

stacking faults (see more details on the role of Mn in the stacking fault formation in Note S3).

In accord with expectation, the faulting observed in the TEM images (Figure 5) leads to an appearance of potential barriers. To demonstrate this relationship, we exposed the interior of a single ZnS:Mn microparticle by etching with FIB (see Methods). As can be seen in Figure 6a, the MP subjected to ion bombardment contains two areas with distinct structure, which are the result of coupling between material heterogeneous properties and the ion beam/material interaction[61,62] (for details on formation of the FIB-induced ripple pattern see Note S4). We then probed the surface potential of the FIB-exposed stacking fault areas with Kelvin probe force microscopy (KPFM) (see Methods). To avoid KPFM artifacts related to imaging of abrupt topological changes,[63] we picked flat areas of the sample without FIB-induced ripples for KPFM imaging experiments (*e.g.*, red rectangle in Figure 6a). The potential difference measured by KPFM is shown in Figure 6b and indicates the presence of bands of 10−100 nm width with alternating surface potential as predicted for faulted ZnS crystals.[41,47] Importantly, these bands do not overlap with the surface topography (Figure 6c). Even though quantitative analysis of the potential barrier heights (Figure 6d) may be inaccurate for the FIB-treated sample under ambient conditions,[64] the relative values can be used to confirm the presence of built-in fields and are in good agreement with barrier heights predicted by DFT.[52,65]

ZnS:Mn Nanocrystals without Stacking Faults and Dislocations Do Not Emit ML. The above optical and structural studies of the faulted ZnS:Mn microparticles strongly imply that ML originates from the MP areas with high concentration of dislocations and stacking faults. It is desirable to directly confirm that these defects are necessary for the ML. The most obvious approach would be to synthesize and test defect-free wurtzite ZnS:Mn microparticles. However, in the method used to prepare the samples for the present study,[5,23] extended defects are inevitably introduced during the cooling process following the solid-state reaction above the temperature of transition from zinc blende to wurtzite in ZnS.[40,60] Thus, as the closest possible alternative, we synthesized ZnS:Mn nanocrystals without stacking faults and dislocations (Figure S23, Methods). ML tests (Figure S23d) confirm that defect-free nanocrystals do not emit ML under a compressive pressure up to 200 MPa. This result is fully consistent with a critical role for defects in the production of ML in elastic and plastic regimes. We also note that ML has been reported previously for ZnS:Mn nanocrystals with diameters in the range of 2−5 nm,[66] which likely excludes the presence of the structural defects. Authors attributed this effect to fracto-mechanoluminescence induced by impulsive deformation. When taken together, Sharma *et al.*'s and our study provide a coherent picture in which ML can be produced from ZnS:Mn in the absence of structural defects only by fracturing the material.

Mechanism of Elastic Piezo-phototronic ML Excitation in ZnS:Mn. The present single-particle ML studies reveal the existence of three distinct ML mechanisms, which we ascribe to elastic piezo-phototronic mechanoluminescence (the Pz-mechanism) and deformation mechanoluminescence due to fully or quasi-reversible dislocation bowing (the μD-mechanism) and, at higher pressures, irreversible dislocation glide (the D-mechanism). At the lowest pressures below 8.1 MPa, which are of the most interest to us, the ML production is dominated by the Pz-mechanism. At this pressure range, the Pz- and μD-mechanisms can operate simultaneously but have a different structural basis. μD-ML is excited by moving dislocations.[13,17] For the Pz-ML, we propose that ML excitation is sourced in the stacking faults (see Figure 5 and the following subsection for the model).

Even though the Pz-ML is distinct from the μD−D-ML by numerous criteria (*e.g.*, statistics of the energy distributions (Figure 3) and ML spatiotemporal patterns (Figures 2 and 4)), our data do not allow completely ruling out the deformation mechanism for the Pz-components in Figure 2. At the same time, the existence of the piezo-phototronic mechanism is strongly supported by the experiments, in which ML was excited by hydrostatic pressure,[26,27,67] the conditions excluding dislocation motion.

Irrespective of these considerations, the elastic piezo-phototronic mechanoluminescence represents an interesting case for theoretical elucidation of the underlying mechanism. Knowing such a mechanism would lead to immediate empirical implications, because excitation of mechanoluminescence exclusively by a strictly elastic process can provide a predictable, calibratable response as demanded in force-sensing applications.

Current descriptions of low-pressure elastic ZnS:Mn mechanoluminescence as piezoelectrically induced electroluminescence solely rely on a piezoelectric effect in the phase-pure WZ ZnS host.[2,3,5,10,68] However, such a mechanism cannot explain the observation presented here, specifically ML excitation by a pressure of <1 MPa. In the absence of exciting light or current, ML carriers cannot originate from the valence band; rather they must be stored in traps that are not thermally emptied. However, the estimation for the band bending induced by a typical ML threshold pressure of 1 MPa is only 0.02 meV/unit cell. Yet a trap with a depth of less than kT cannot remain filled at room temperature in the steady state. Hence, the internal electric field induced by a deformation is insufficient to account for the observations by orders of magnitude. The insufficiency of piezoelectric polarization for ML excitation is also supported by the fact that we do not observe ML in defect-free ZnS:Mn nanocrystals.

Here we present a model for elastic mechanoluminescence of ZnS:Mn that depends upon the presence of much larger internal electric fields that necessarily accompany deformations in the presence of stacking faults (Figure 7). It relies on the very well-known tendency of ZnS to produce superlattices of alternating hexagonal and cubic crystal phases of differing thickness, leading to the presence of strong built-in electric fields.[41] In accord with our experimental observations, this mechanism can be spatially localized and can coexist with deformation mechanoluminescence.

ZnS is a highly n-type semiconductor with residual electron density $n \approx 10^4$ cm^{-3} at 300 K, which is significantly higher than expected for thermally ionized carriers in a wide-band-gap material.[69] This is characteristic of a compensated semiconductor with a high concentration of donor and acceptor defect states,[70] $N_d \gg N_a \approx 10^{18}$ cm^{-3}. In the absence of an external field, most donors are filled with electrons and have neutral charge D^0, whereas material charge neutrality is maintained by the small fraction of ionized donors D^+ compensating for the filled acceptors A^-, $N_d^+ = N_a^-$.

In the faulted structure, such as shown in Figure 7a, the electric field in the hexagonal phase E_{WZsp} arises due to the lack of inversion symmetry along the c-axis. When the cubic phase is inserted between two hexagonal segments, it acquires the opposite directed field $E_{ZBpiezo}$ due to the inverse piezoelectric effect.[71] Hence, a built-in sawtooth potential Ψ_{saw} is created,[52] and free carriers (electrons) drift toward the positive pole, leaving emptied D^+ and A^0 levels to compensate for the built-in field. The most likely candidates for A^0 centers are shallow hole states residing 62 meV above the valence band at sulfur vacancies, which are known to participate in defect-related ZnS luminescence at room temperature.[72]

Each interface between the phases contains a built-in potential barrier $\Psi_{bi} = \Psi_{offset} + \Psi_{saw} - \Psi_{screen}$, where Ψ_{offset} is a type-II band offset between WZ and ZB phases ($\Psi_{offset}^{CB} = 57$ meV, $\Psi_{offset}^{VB} = 33$ meV[73]), Ψ_{saw} depends on the relative sizes of WZ and ZB phases and is estimated to be >400 meV/10 nm,[52] and Ψ_{screen} is a double depletion layer on both sides of each interface that arises due to compensation for Ψ_{saw}. An additional contribution to the potential difference can arise due to the presence of piezoelectrically induced interfacial strain and concurrent flexoelectric effect[43,74] as well as extended defects. Importantly, the WZ/ZB/WZ sequence shown in Figure 7 represents the nanoscale structural unit of our model where lateral sizes of the phases along the c-axis define the heights of the built-in potential barriers and, consequently, the degree of compensation. In the model presented here, this preexisting electrical structure plays a crucial role in the appearance of ML. As discussed in the previous section, the high tendency to produce stacking faults is distinctive to the ternary ZnMnS system if prepared by the conventional methods such as the solid-state reaction.[5,23] Nanotechnological approaches offer an exciting possibility to extend the piezo-phototronic mechanism to other II−VI and III−V semiconductors by preparing these materials with a high concentration of stacking faults.

The above value of Ψ_{offset} is estimated for the 2H/3C interface. This combination produces the highest potential barrier since 2H modification has maximum hexagonality.[56] However, a distribution of 6H, 4H, and 2H modifications can exist in the crystals, whereas the ZB phase has only 3C modification.[41] In combination with size-dependable Ψ_{saw}, it gives a wide distribution for the heights of Ψ_{bi}, leading to heterogeneity in the threshold pressure for ML appearance, which is not predicted by the previously described mechanisms (see introductory section), but observed by us in the experiments (Figure 1d).

Upon compression (Figure 7b), a unidirectional piezoelectric field is established across the whole particle. It coincides with the built-in field direction in the cubic phases and opposes the built-in field in the hexagonal phases. The total internal fields rearrange accordingly, leading to the changes in Ψ_{bi}. The most pronounced change is at the ZB/WZ interface, which is electron depleted due to intrinsic compensation for the built-in fields. Here the stress-induced potential profile Ψ_{piezo} cannot be screened by free electrons, and bands of both WZ and ZB phases can include opposing potential jumps similarly to a piezoelectric p−n junction.[68,75] Thus, the resulting increase in the local potential barrier can be significantly higher than the one predicted by the intrinsic WZ phase ZnS piezoelectric coefficient alone.

If the piezoelectric field induced by mechanical deformation along the *c*-axis is greater than the built-in field $E_{\mathrm{piezo}} \geqslant E_{\mathrm{bi}}$, free electrons are released from the potential well at the WZ/ZB interface and can acquire enough kinetic energy to reach the bottom of the conduction band in the WZ phase and recombine with holes at the A^0 centers (see Figure 7b). Energy, released after recombination of the accelerated electron with the hole, can with very high probability be nonradiatively transferred to a neighboring isoelectric Mn^{2+} impurity at a Zn position[76] followed by its excitation and radiation of a quantum of 585 nm light:

$$e^- + A^0 \rightarrow (A^-)^* \tag{1}$$

$$(A^-)^* + \mathrm{Mn}^{2+} \rightarrow A^- + (\mathrm{Mn}^{2+})^* \tag{2}$$

$$(\mathrm{Mn}^{2+})^* \xrightarrow{h\nu} \mathrm{Mn}^{2+} \tag{3}$$

The above process can produce an instantaneous ML peak. The model can also account for the delayed ML peaks, which are not observed in the present study likely due to limitations of the experimental setup. The delayed peaks are produced when $E_{\mathrm{piezo}} < E_{\mathrm{bi}}$ and can be understood in terms of delayed recombination (Figure S24):

$$e^-_{\mathrm{VB}} + A^0 \rightarrow A^- + [h^+_{\mathrm{VB}}]_{\mathrm{ZB/WZ}} \tag{4}$$

$$e^- + D^+ \rightarrow D^0 \tag{5}$$

Upon pressure release:

$$h^+_{\mathrm{VB}} + \mathrm{Mn}^{2+} \rightarrow (h^+, \mathrm{Mn}^{2+}) \tag{6.1}$$

$$D^0 \rightarrow D^+ + e^- \tag{6.2}$$

$$D^0 + (h^+, \mathrm{Mn}^{2+}) \rightarrow D^+ + (\mathrm{Mn}^{2+})^* \tag{7.1}$$

Or

$$e^- + (h^+, \mathrm{Mn}^{2+}) \rightarrow (X, \mathrm{Mn}^{2+}) \rightarrow (\mathrm{Mn}^{2+})^* \tag{7.2}$$

Or

$$e^- + h^+_{\mathrm{VB}} \rightarrow X;\ X + \mathrm{Mn}^{2+} \rightarrow (X, \mathrm{Mn}^{2+}) \rightarrow (\mathrm{Mn}^{2+})^* \tag{7.3}$$

$$(\mathrm{Mn}^{2+})^* \xrightarrow{h\nu} \mathrm{Mn}^{2+} \tag{8}$$

In this case, at the moment of stress application holes trapped at the A^0 centers due to intrinsic compensation can be captured into the potential well produced at the ZB/WZ interface by the piezoelectrically induced potential jump (4). Simultaneously, some of the donor centers in the ZB phase can be repopulated with electrons during the reverse compensation in response to the onset of piezoelectric polarization (5). Subsequent release of stress is followed by disappearance of these potential jumps and the release of holes to the valence band. Holes h^+_{VB} then can be bound by a nearby hole-attractive Mn^{2+} ion (6.1), which can be excited *via* various routes,[77] as schematically shown at the steps (6) and (7) above. Mn excitation can involve recombination between electron at the D^0 center and the hole trapped at the neighboring Mn center (7.1) or release of the electron from the D^0 center due to recompensation (6.2) and formation of the exciton X bound to the Mn^{2+} ion (7.2 or 7.3). After resonant transfer of electron−hole or exciton recombination energy to a Mn, the excited Mn^{2+} ion returns to the ground state *via* emission of the well-known orange light. ML excitation during the dilation of ZnS:Mn MPs shown in Figure 7c is expected to be very similar to the process described above for the compression except for the reversed role of the ZB and WZ phases.

As can be seen from the above discussion, the ML process governed by the proposed mechanism is reversible in terms of the mechanical subsystem of the crystal but not in terms of its electronic subsystem. The behavior of the real system is more complicated than this. The ML process consumes the electrons participating in compensation for the built-in fields so that Ψ_{screen} decreases (Figure 7d). Potential jumps produced at the next pressure cycle become bigger and electrons can more easily escape the potential well at the WZ/ZB interface. This explains the initial increase of intensity observed by us in the Pz-components (Figure 2c and f). In addition, the consumption of the carriers leads to a decrease of charge at the WZ/ZB interface, which can be considered as a partial dislocation. It is well known that the electronic subsystem of II−VI semiconductors is in strong mutual interaction with their 1D and 2D defects such as dislocations and stacking faults.[16] In particular, a decrease of dislocation charge increases their mobility. Hence, one can conclude that each cycle of elastic ML excitation increases the chances of an elastic or microplastic event at the WZ/ZB interface at the next pressure cycle and subsequent appearance of the μD-component. Finally, the internal reservoir of the carries is depleted and ML stops.

CONCLUSION

We have developed a method for reliable detection of mechanoluminescence of single ZnS:Mn microparticles. A single-particle study has uncovered complex spatiotemporal patterns, dynamics, and heterogeneity in the threshold pressure for ML appearance, which inevitably have been averaged out in previous multiparticle experiments. This discovery has led us to distinguish two distinct ML mechanisms, namely, elastic piezo-phototronic and dislocation-related. The latter mechanism can be further subdivided into elastic-microplastic mechanoluminescence attributable to fully or quasi-reversible dislocation bowing, and plastic mechanoluminescence governed by glide of the unpinned dislocations. At low pressures, two mechanisms can operate simultaneously but with different structural bases.

We provide arguments, based on statistical analysis of the ML pulse energy distributions, to further support the distinct physical nature of the piezo- and dislocation-related mechanisms. We use nanoscale structural characterization in conjunction with analysis of ML spatiotemporal patterns to demonstrate the connection between the elastic piezo-phototronic mechanoluminescence in the ZnS:Mn microparticles and their internal structure, particularly with the presence of multiple stacking faults, concomitant built-in electric fields and potential barriers.

On the basis of this observation, we propose a mechanism for elastic low-force ZnS:Mn mechanoluminescence, which relies on the special electrical properties of the interfaces between two distinct crystal phases within the microparticle volume. Some of these interfaces are electron-depleted, which leads to the local enhancement of the piezoelectric field generated during the application of external stress. In contrast to previous models, our mechanism provides an explanation for extremely low pressures (as low as 233 kPa) sufficient for excitation of mechanoluminescence in ZnS:Mn. An important consequence of this mechanism is its scalability to the nanoscale. TEM data show that ZB inclusions can be very small (2 nm), implying that the ML structural unit (the WZ/ZB/WZ sequence) can be scaled down to 100 nm and below. Potentially, this enables creation of miniature nanoscale stress sensors as demanded in both technological and biomedical applications.

MATERIALS AND METHODS

Mechanoluminescence Detection. The MPs are spin-coated from a methanol suspension on a thin glass coverslip of 1 cm diameter rigidly mounted in plastic dish. The dish is fixed at the sample holder of an inverted wide-field microscope (Nikon Eclipse Ti2) equipped with a 100× CFI Plan Apo Lambda objective, PFS, and EMCCD camera (Andor iXon Ultra 888). Nikon's PFS uses reflected light of 870 nm LED to detect changes in the z position of the coverslip and adjusts the position of the objective to maintain focus in real time (see Figure 1b). If the z position of the coverslip is changed due to application of pressure, there is a 30−300 ms lag between the moment of pressure application and the moment when the change in z position is detected. The amount of lag depends on the amplitude of the applied pressure. All time-resolved ML curves are corrected for the lag; the exact amount is defined based on comparison of time-resolved curves of photoexcited luminescence and pressure at the moment of pressure release. More details are provided in Note S1 and Figure S2. The z position is read out and saved during acquisition of each ML frame every 0.633−20 ms depending on the ML acquisition time, which is varied in the range 0.633−300 ms. Thus, the z position is measured 1−6 times per frame. ML emission is detected by an EM CCD camera. Before reaching the detector, ML light passes through a 570−620 nm bandpass filter, which cuts off 870 nm light of the PFS LED. Analog-Digital Units (ADUs) reported by the camera are further converted to photons using the following relation:

$$\text{Photons} = \frac{(\text{ADU} - \text{biasoffset}) \times \text{preamp}}{\text{EM gain} \times \text{QE}}$$

where the bias offset is set to 100, preamp = 5.72 is the preamplification gain under the chosen imaging settings, EM gain is chosen for each experiment, and QE = 0.95 at 595 nm is the quantum efficiency of the camera sensor. For each data set, ML roi is chosen manually using the sum projection of the stack of 2D ML images. ML intensity per frame is then calculated by integrating over the ML roi and subtracting the background level. The background level is established by integrating over the same ML roi stack of dark frames.

A needle with a flat tip of 3.5 μm diameter is mounted in the holder of a Signatone S 926 micropositioner and used to apply compressive deformation to the MPs and, consequently, to excite ML flashes. The pressure can be applied by adjusting the z knob of the micropositioner, or the micropositioner with the probe can be firmly mounted on a PI P-611.3 NanoCube piezoelectric nanopositioner, which is programmed to generate periodic changes in the z position of the probe relative to the coverslip. In the latter case, periodic pressure pulses are produced when the piezoelectrically driven needle comes into contact with the coverslip. In the experiments involving cyclic loading, the individual MPs are glued to the epoxy- or PDMS-covered tip of the probe needle. Pressure pulse generation is synchronized with ML acquisition by sending the transistor−transistor logic (TTL) pulse from the camera to the nanopositioner at the beginning of the acquisition.

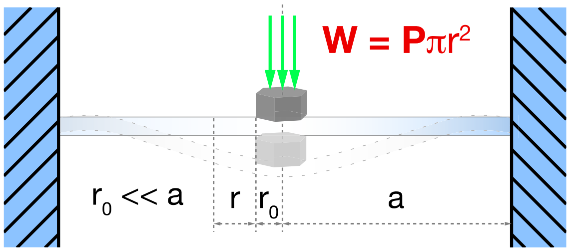

Pressure applied to the MPs causes deflection of the coverslip, which is detected by the PFS. The objective is then moved to correct for the deflection with a precision of 10 nm. We use a home-written Matlab script to simultaneously record alterations in the z position of the coverslip as reported by the PFS and 2D images of ML flashes. The pressure is measured based on the deflection of the coverslip Δz, which is converted to pressure using a model for the deflection of a centrally loaded circular plate with fixed support.[78] Under the assumption that the maximum deflection is not more than about one-half the thickness of the plate, a uniform load W over a very small central area of radius r_0 (diameter of the tip or the particle, whichever is smaller) at $r = 0$ is connected to the deflection as follows:

$$\Delta z = \frac{-Wa^2}{16\pi D}$$

where $W = P\pi r^2$ is the total load applied to the plate, P is pressure, r is equivalent radius of loading, a is the radius of the plate, and D is the plate constant. $D = \frac{Et^3}{12(1-\nu^2)}$, where E is the modulus of elasticity, t is the thickness of the plate, and ν is Poisson's ratio. Equivalent radius r accounts for concentrated loading and depends largely upon the thickness of the plate t: $r = \sqrt{1.6r_0^2 + t^2} - 0.675t$ if $r_0 < 0.5t$. The uncertainty range is determined by the precision of Nikon's PFS system and is calculated to be ±60 kPa.

ZnS:Mn Microparticles. The powder samples of ZnS:Mn microparticles with 0.9 at. % Mn^{2+} ions were received from the laboratory of Prof. Caofeng Pan at Beijing Institute of Nanoenergy and Nanosystems. The samples were prepared *via* a high-temperature solid-state reaction.[31] These materials were washed with acetone and isopropanol and studied with no further modification.

Statistical Analysis of Distributions of the Energies of ML Pulses. Statistical analysis of distributions of the energies of ML pulses is based on the method described in ref 38. In the first step, experimental data sets were binned using either a linear scheme, with $b_i = E_{\min} i$, where $E_{\min}$ is the minimum energy value of a data set, or a logarithmic scheme, with $b_i = C \times 2^{(i-1)}$, where C is chosen to provide optimal resolution; the same C is used for all data sets belonging to the same particle. The usage of the linear binning scheme was beneficial for the Pz-components because of the relatively small spread of the data, whereas E values of the μD−D-components span over 4 orders of magnitude and require the logarithmic scheme.

In the next step, five parametrized models are fitted to the binned data sets using the method of maximum likelihood.[79] The models include the power law, stretched exponential, log-normal, and, as controls, power laws with exponential cutoffs and exponentials. The definitions of the models are given in Table S1. Each fitting procedure results in estimates of parameters, as well as the p-value for the goodness of fit. The Kolmogorov—Smirnov test as a distance measure between data and the fitted model was used for the determination of the goodness of fit. The test was performed using a home-written Matlab script made available in ref 80. The models that had p-values less than 0.1 were rejected.

Finally, the models with the goodness of fit above the threshold of 0.1 were compared against each other using the log-likelihood ratio test, which estimates the ratio of the likelihoods of the binned data H for the pair of models A and B:

$$\mathcal{R} = \ln\left(\frac{\mathcal{L}_A(H|\theta_A)}{\mathcal{L}_B(H|\theta_B)}\right)$$

, where θ are best fit parameters for each model. Positive and negative $\mathcal{R}$ support models A and B, respectfully. The sign of $\mathcal{R}$ can be trusted only if the p-value calculated for the log-likelihood ratio test is smaller than 0.1.

Control distributions, *viz.*, the power law with an exponential cutoff and exponential distribution, were excluded by the goodness of fit and log-likelihood ratio tests for example 1 in Figure 2c (Tables S2 and S3) and received no or weak support for example 2 in Figure 2f (Tables S4 and S5).

AFM. Atomic force microscopy (AFM) was performed in AC/tapping and KPFM modes with a Cypher S instrument using soft, Ti/Pt (5/20)-coated electri-levers with a frequency of 70 kHz and a spring constant of 2 N/m (Asylum Research, Santa Barbara, CA, USA). The ZnS:Mn particles were dispersed in pure isopropanol by sonication followed by centrifugation before drop casting onto highly conductive silicon substrates and dried on a hot plate at 55 °C for 5 min (Silicon Quest International, San Jose, CA, USA). The KPFM images were collected with a lift height of 20 nm and a 3 V AC drive amplitude to induce an electrostatic force between the tip and the sample.

SEM. Scanning electron microscopy was performed on the same ZnS:Mn sample that was used for AFM and KPFM analysis using a Zeiss Ultra55 FESEM instrument (Carl Zeiss Microscopy, Thornwood, NY, USA). All images were collected with an accelerating voltage of 4 keV and using the in-lens secondary electron detector.

FIB. TEM specimens were prepared using an FEI Helios 660 dual-beam FIB/SEM, following standard lift-out procedures. Protective layers of carbon (electron-beam-assisted deposition) followed by platinum (focused-ion-beam-assisted deposition) were deposited over areas of a microparticle chosen to include at least one stacking fault, as determined by SEM. Ion milling was carried out at 30 kV with currents of 2.5 nA, 150 pA, and 40 pA. Final sample cleanup was carried out in a Fischione 1040 Nanomill using Ar at 500 eV and 180 pA.

FIB ion milling with the same voltage/current settings was also used to expose the interior of MPs to provide KPFM images of the particles' internal structure.

TEM. TEM, electron diffraction, and HRTEM were performed on an FEI Tecnai T20 S-twin TEM operating at 200 keV with a LaB6 filament. The FIB-prepared sample was loaded in an FEI double-tilt TEM holder and aligned to the desired zone axes using the diffraction pattern. TEM images and diffraction patterns were collected using a Gatan Rio 16 camera using the drift correction feature, which collects images at 20FPS, calculates the drift between subsequent images, removes the drift, and sums the images. Diffraction contrast images were collected with a 30 μm objective aperture, and HRTEM images were collected without an objective aperture. Image analysis was done in Gatan Digital Micrograph 3.0 (GMS 3.0). For all FFTs displayed and analyzed care was taken to avoid streaking artifacts that result from image edges. Briefly in GMS 3.0, a 2^n by 2^n pixel area of interest was cropped from the image and was subsequently multiplied by a 2D Hanning window followed by computing the FT. For visualization, the log of the modulus of the FT was saved and visualized in ImageJ using the "fire" lookup table to facilitate viewing. For electron diffraction patterns, the log of the intensity was calculated to allow weaker peaks to be visible. Electron diffraction patterns were simulated using the CryTBox software.[81]

Synthesis of ZnS:Mn Nanocrystals. In a typical synthesis, 1.5 g of zinc stearate, 15 mg of anhydrous $MnCl_2$, 25 mL of oleylamine, and 25 mL of dodecanethiol were combined in a 100 mL three-neck flask equipped with a water-cooled condenser. The reaction mixture was degassed at 100 °C for 1 h and heated to 300 °C under an argon flow. Refluxing at this temperature for 45 min yielded 7.8 ± 3.7 nm nanocrystals. The reaction was stopped by removal of the heating mantle. After reaching room temperature, the reaction mixture was crashed by addition of an excess of ethanol. The precipitate was washed three times using hexane/ethanol as the solvent/nonsolvent.

EDS Mapping. High-angle annular dark field (HAADF) STEM and STEM EDS maps were collected on an FEI TitanX 60-300 microscope at the National Center for Electron Microscopy, Molecular Foundry, Lawrence Berkeley National Laboratory. An FEI low-background double-tilt holder was used for all experiments. Samples were aligned to the $[11\bar{2}0]$ zone axis using the diffraction pattern. HAADF STEM was performed at 200 kV with a beam convergence semiangle of 10 mrad using a Fischione HAADF detector. STEM-EDS mapping was performed at 200 kV with a typical probe current of ~450 pA using an FEI Super-X Quad windowless detector with a solid angle of 0.7 steradians. Data were collected using the Bruker Esprit software utilizing drift correction. Quantification was performed using the Bruker Esprit software using the Cliff−Lorimer method. Maps were averaged until the Mn signal could be clearly resolved from the bremsstrahlung background in a spectrum averaged over the whole scan area (~30−45 min).

ASSOCIATED CONTENT

Supporting Information

The Supporting Information is available free of charge at https://pubs.acs.org/doi/10.1021/acsnano.0c08890.

Figure S1 shows XRD data; Note S1 and Figure S2−S4 describe the use of Nikon's PFS to detect pressure; Figure S5 shows scaling of ML total counts with particles' diameter; Figure S6 shows ML excited by different probes and in different media; Note S2 describes the factors affecting ML repeatability; Figures S7−S9 show time-resolved ML of single microparticles; Figure S10 presents the results of ML excitation with decreasing pressure amplitude; Figure S11 shows the width of ML pulses; Figures S12−S14 and Tables S1−S5 include statistical data on distributions of energy released by the ML process; Figures S16 and S17 show PL images of microparticles; Note S3 and Figures S18−S20 describe the role of Mn in the ML process; Figures S21 and S22 show HRTEM images of microparticles; Note S4 explains the formation of FIB patterns; Figure S23 shows data on ML excitation in the ensemble of ZnS:Mn nanocrystals; Figure S24 shows an energy band diagram illustrating the model described in the text (PDF)

Supporting movie S1 shows the piezo-phototronic ML, also shown in Figure 2f-h (AVI)

Supporting movie S2 shows the deformation ML, aslo shown in Figure 2a-e (AVI)

Supporting movie S3 shows the deformation ML for another MP (AVI)

Supporting movie S4 shows ML due to dislocation bowing, a particular case of the deformation ML, also shown in Figure 2f-h(AVI)

Supporting movie S5 shows the piezo-phototronic ML recorded with high temporal resolution, also shown in Figure 4 (AVI)

AUTHOR INFORMATION

Corresponding Authors

Maria V. Mukhina − *Department of Molecular and Cellular Biology, Harvard University, Cambridge, Massachusetts 02138, United States*; orcid.org/0000-0001-9656-1221; Email: mmukhina@fas.harvard.edu

Nancy Kleckner − *Department of Molecular and Cellular Biology, Harvard University, Cambridge, Massachusetts 02138, United States*; Email: kleckner@fas.harvard.edu

Authors

Jason Tresback − *Center for Nanoscale Systems, Harvard University, Cambridge, Massachusetts 02138, United States*

Justin C. Ondry − *Department of Chemistry, University of California, Berkeley, California 94720, United States*; orcid.org/0000-0001-9113-3420

Austin Akey − *Center for Nanoscale Systems, Harvard University, Cambridge, Massachusetts 02138, United States*

A. Paul Alivisatos − *Department of Chemistry, University of California, Berkeley, California 94720, United States; Materials Sciences Division, Lawrence Berkeley National Laboratory, Berkeley, California 94720, United States; Department of Materials Science and Engineering, University of California, Berkeley, California 94720, United States; Kavli Energy NanoScience Institute, Berkeley, California 94720, United States*; orcid.org/0000-0001-6895-9048

Complete contact information is available at: https://pubs.acs.org/10.1021/acsnano.0c08890

Notes

The authors declare no competing financial interest.

ACKNOWLEDGMENTS

The authors thank Prof. Zhong Lin Wang and Prof. Caofeng Pan, who kindly provided the sample of ZnS:Mn microparticles used in this study. The primary part of this work was supported by National Institutes of Health (NIH) grants R01GM025326 and R35GM136322. Parts of this study were performed at the Harvard University Center for Nanoscale Systems (CNS), which is a member of the National Nanotechnology Coordinated Infrastructure Network (NNCI) and supported by the National Science Foundation under NSF award no. 1541959. Also the study was supported by the National Science Foundation, Division of Materials Research (DMR), under award number DMR-1808151. J.C.O. gratefully acknowledges the support of the Chevron-UC Berkeley Graduate Student Fellowship. Work at the Molecular Foundry was supported by the Office of Science, Office of Basic Energy Sciences, of the U.S. Department of Energy under contract no. DE-AC02-05CH11231. We would like to thank Prof. Vladimir Maslov for discussion, review, advice, and useful comments on the mechanism of ZnS:Mn mechanoluminescence.

REFERENCES

(1) Walton, A. J. Triboluminescence. *Adv. Phys.* **1977**, *26*, 887−948.

(2) Feng, A.; Smet, P. F. A Review of Mechanoluminescence in Inorganic Solids: Compounds, Mechanisms, Models and Applications. *Materials* **2018**, *11*, 484.

(3) Zhang, J.-C.; Wang, X.; Marriott, G.; Xu, C.-N. Trap-Controlled Mechanoluminescent Materials. *Prog. Mater. Sci.* **2019**.

(4) Meyer, K.; Obrikat, D.; Rossberg, M. Progress in Triboluminescence of Alkali Halides and Doped Zinc Sulphides (i). *Krist. Tech.* **1970**, *5*, 5−49.

(5) Wang, X.; Zhang, H.; Yu, R.; Dong, L.; Peng, D.; Zhang, A.; Zhang, Y.; Liu, H.; Pan, C.; Wang, Z. L. Dynamic Pressure Mapping of Personalized Handwriting by a Flexible Sensor Matrix Based on the Mechanoluminescence Process. *Adv. Mater.* **2015**, *27*, 2324−2331.

(6) Bhargava, R.; Gallagher, D.; Hong, X.; Nurmikko, A. Optical Properties of Manganese-Doped Nanocrystals of ZnS. *Phys. Rev. Lett.* **1994**, *72*, 416.

(7) Beaulac, R.; Archer, P. I.; Ochsenbein, S. T.; Gamelin, D. R. Mn^{2+}-Doped CdSe Quantum Dots: New Inorganic Materials for Spin-Electronics and Spin-Photonics. *Adv. Funct. Mater.* **2008**, *18*, 3873−3891.

(8) Xu, C.; Watanabe, T.; Akiyama, M.; Zheng, X. Artificial Skin to Sense Mechanical Stress by Visible Light Emission. *Appl. Phys. Lett.* **1999**, *74*, 1236−1238.

(9) Gumlich, H.-E. Electro- and Photoluminescence Properties of Mn^{2+} in ZnS and ZnCdS. *J. Lumin.* **1981**, *23*, 73−99.

(10) Tiwari, R.; Dubey, V.; Chandra, B. Exact Model for the Elastico Mechanoluminescence of II−VI Phosphors. *Mater Phys. Mechan.* **2014**, *19*, 25−38.

(11) Sohn, K.-S.; Timilsina, S.; Singh, S. P.; Choi, T.; Kim, J. S. Mechanically Driven Luminescence in a ZnS:Cu-PDMS Composite. *APL Mater.* **2016**, *4*, 106102.

(12) Nickolayev, O.; Petrenko, V. F. Study of Dislocations in ZnSe and ZnS by Scanning Force Microscopy. *J. Vac. Sci. Technol., B: Microelectron. Process. Phenom.* **1994**, *12*, 2443−2450.

(13) Alzetta, G.; Chudáček, I.; Scarmozzino, R. Excitation of Triboluminescence by Deformation of Single Crystals. *physica status solidi (a)* **1970**, *1*, 775−785.

(14) Bredikhin, S. I.; Shmurak, S. Z. The Luminescence and Electrical Characteristics of ZnS Crystals Undergoing Plastic Deformation. *Sov. Phys. JETP* **1977**, *46*, 768−73.

(15) Bredikhin, S. I.; Shmurak, S. Z. Deformation Luminescence in II−VI Crystals. *J. Phys. Colloq.* **1983**, *44*, 183−188.

(16) Osip'yan, Y. A.; Petrenko, V. F.; Zaretskii, A. V.; Whitworth, R. W. Properties of II-VI Semiconductors Associated with Moving Dislocations. *Adv. Phys.* **1986**, *35*, 115−188.

(17) Chandra, B. P.; Goutam, R. K.; Chandra, V. K.; Patel, R. P.; Luka, A. K.; Baghel, R. N. Luminescence Induced by Elastic and Plastic Deformation of II−VI Semiconductors at Fixed Strain Rates. *Optoelectron. Adv. Mater.* **2009**, *3*, 1181−1189.

(18) Maaß, R.; Derlet, P. M. Micro-Plasticity and Recent Insights from Intermittent and Small-Scale Plasticity. *Acta Mater.* **2018**, *143*, 338−363.

(19) Suzuki, T.; Takeuchi, S.; Yoshinaga, H. *Dislocation Dynamics and Plasticity*; Springer Series in Materials Science; Springer Science & Business Media: Berlin, 2013; Vol. *12*; p 63 ff.

(20) Levade, C.; Faress, A.; Vanderschaeve, G. A TEM *in Situ* Investigation of Dislocation Mobility in the II−VI Semiconductor Compound ZnS a Quantitative Study of the Cathodoplastic Effect. *Philos. Mag. A* **1994**, *69*, 855−870.

(21) Vardanyan, R. A. Cross Section for Electron Capture by a Charged Dislocation in a Semiconductor. *Sov. Phys. JETP* **1979**, *49*, 1132.

(22) Chandra, B. P.; Chandra, V. K.; Jha, P.; Sonwane, V. D. Threshold Pressure for Mechanoluminescence of Macrocrystals, Microcrystals and Nanocrystals of Doped Zinc Sulphide. *Phys. B* **2016**, *491*, 12−16.

(23) Wang, X.; Que, M.; Chen, M.; Han, X.; Li, X.; Pan, C.; Wang, Z. L. Full Dynamic-Range Pressure Sensor Matrix Based on Optical and Electrical Dual-Mode Sensing. *Adv. Mater.* **2017**, *29*, 1605817.

(24) Qian, X.; Cai, Z.; Su, M.; Li, F.; Fang, W.; Li, Y.; Zhou, X.; Li, Q.; Feng, X.; Li, W.; Hu, X.; Wang, X.; Pan, C.; Song, Y. Printable Skin-Driven Mechanoluminescence Devices *via* Nanodoped Matrix Modification. *Adv. Mater.* **2018**, *30*, 1800291.

(25) Wu, W.; Wang, Z. L. Piezotronics and Piezo-Phototronics for Adaptive Electronics and Optoelectronics. *Nat. Rev. Mater.* **2016**, *1*, 1−17.

(26) Alzetta, G.; Minnaja, N.; Santucci, S. Piezoluminescence in Zinc-Sulphide Phosphors. *Nuovo Cimento* **1962**, *23*, 910−913.

(27) Alzetta, G.; Chella, G.; Santucci, S. Behaviour of Light Emission in Mechanically Excited ZnS Phosphors. *Phys. Lett. A* **1967**, *26*, 94−95.

(28) Yang, H.; Holloway, P. H.; Ratna, B. B. Photoluminescent and Electroluminescent Properties of Mn-Doped ZnS Nanocrystals. *J. Appl. Phys.* **2003**, *93*, 586−592.

(29) Sasakura, H.; Kobayashi, H.; Tanaka, S.; Mita, J.; Tanaka, T.; Nakayama, H. The Dependences of Electroluminescent Characteristics of ZnS:Mn Thin Films upon Their Device Parameters. *J. Appl. Phys.* **1981**, *52*, 6901−6906.

(30) Terasaki, N.; Xu, C.-N. Performance of Single Mechanoluminescent Particle as Ubiquitous Light Source. *J. Colloid Interface Sci.* **2014**, *427*, 62−66.

(31) Wang, X.; Ling, R.; Zhang, Y.; Que, M.; Peng, Y.; Pan, C. Oxygen-Assisted Preparation of Mechanoluminescent Zns:Mn for Dynamic Pressure Mapping. *Nano Res.* **2018**, *11*, 1967−1976.

(32) Sakai, K.; Koga, T.; Imai, Y.; Maehara, S.; Xu, C.-N. Observation of Mechanically Induced Luminescence from Microparticles. *Phys. Chem. Chem. Phys.* **2006**, *8*, 2819−2822.

(33) Osip'yan, Y. A.; Petrenko, V. F. Investigation of the Mechanism of the Motion of Charged Dislocations in ZnSe. *Sov. Phys. JETP* **1978**, *48*, 147.

(34) Richeton, T.; Dobron, P.; Chmelik, F.; Weiss, J.; Louchet, F. On the Critical Character of Plasticity in Metallic Single Crystals. *Mater. Sci. Eng., A* **2006**, *424*, 190−195.

(35) Weiss, J.; Rhouma, W. B.; Richeton, T.; Dechanel, S.; Louchet, F.; Truskinovsky, L. From Mild to Wild Fluctuations in Crystal Plasticity. *Phys. Rev. Lett.* **2015**, *114*, 105504.

(36) Ispánovity, P. D.; Laurson, L.; Zaiser, M.; Groma, I.; Zapperi, S.; Alava, M. J. Avalanches in 2D Dislocation Systems: Plastic Yielding Is Not Depinning. *Phys. Rev. Lett.* **2014**, *112*, 235501.

(37) Sornette, D. Probability Distributions in Complex Systems. 2007, arXiv:0707.2194. arXiv.org e-Print archive. https://arxiv.org/abs/0707.2194 (accessed December 24, 2020).

(38) Virkar, Y.; Clauset, A. Power-Law Distributions in Binned Empirical Data. *Ann. Appl. Stat.* **2014**, *8*, 89−119.

(39) Malevergne, Y.; Pisarenko, V.; Sornette, D. Empirical Distributions of Stock Returns: Between the Stretched Exponential and the Power Law? *Quant Finance* **2005**, *5*, 379−401.

(40) Sebastian, M. T.; Krishna, P. *Random, Non-Random, and Periodic Faulting in Crystals*; Routledge: New York, 2014; pp 1−366.

(41) Steinberger, I. Polytypism in Zinc Sulphide. *Prog. Cryst. Growth Charact.* **1983**, *1−4*, 7−54.

(42) Neumark, G. F. Theory of the Anomalous Photovoltaic Effect of ZnS. *Phys. Rev.* **1962**, *125*, 838.

(43) Jing, L.; Kershaw, S. V.; Kipp, T.; Kalytchuk, S.; Ding, K.; Zeng, J.; Jiao, M.; Sun, X.; Mews, A.; Rogach, A. L.; Gao, M. Insight into Strain Effects on Band Alignment Shifts, Carrier Localization and Recombination Kinetics in CdTe/CdS Core/shell Quantum Dots. *J. Am. Chem. Soc.* **2015**, *137*, 2073−2084.

(44) Qteish, A.; Heine, V.; Needs, R. Polarization, Band Lineups, and Stability of SiC Polytypes. *Phys. Rev. B: Condens. Matter Mater. Phys.* **1992**, *45*, 6534.

(45) Wenzien, B.; Käckell, P.; Bechstedt, F.; Cappellini, G. Quasiparticle Band Structure of Silicon Carbide Polytypes. *Phys. Rev. B: Condens. Matter Mater. Phys.* **1995**, *52*, 10897.

(46) Daulton, T.; Bernatowicz, T.; Lewis, R.; Messenger, S.; Stadermann, F.; Amari, S. Polytype Distribution of Circumstellar Silicon Carbide: Microstructural Characterization by Transmission Electron Microscopy. *Geochim. Cosmochim. Acta* **2003**, *67*, 4743−4767.

(47) Sebastian, M.; Krishna, P. Anomalous Photovoltaic Effect and Disorder in ZnS Crystals. *Bull. Mater. Sci.* **1983**, *3−4*, 257−266.

(48) Spirkoska, D.; Arbiol, J.; Gustafsson, A.; Conesa-Boj, S.; Glas, F.; Zardo, I.; Heigoldt, M.; Gass, M. H.; Bleloch, A. L.; Estrade, S.; Kaniber, M.; Rossler, J.; Peiro, F.; Morante, J. R.; Abstreiter, G.; Samuelson, L.; Morral, A. F. Structural and Optical Properties of High Quality Zinc-Blende/Wurtzite GaAs Nanowire Heterostructures. *Phys. Rev. B: Condens. Matter Mater. Phys.* **2009**, *80*, 245325.

(49) Heiss, M.; Conesa-Boj, S.; Ren, J.; Tseng, H.-H.; Gali, A.; Rudolph, A.; Uccelli, E.; Peiró, F.; Morante, J. R.; Schuh, D.; Reiger, E.; Kaxiras, E.; Arbiol, J.; Morral, A. F. Direct Correlation of Crystal Structure and Optical Properties in Wurtzite/Zinc-Blende GaAs Nanowire Heterostructures. *Phys. Rev. B: Condens. Matter Mater. Phys.* **2011**, *83*, 045303.

(50) Dick, K. A.; Thelander, C.; Samuelson, L.; Caroff, P. Crystal Phase Engineering in Single InAs Nanowires. *Nano Lett.* **2010**, *10*, 3494−3499.

(51) Liu, M.; Jing, D.; Zhou, Z.; Guo, L. Twin-Induced One-Dimensional Homojunctions Yield High Quantum Efficiency for Solar Hydrogen Generation. *Nat. Commun.* **2013**, *4*, 2278.

(52) Zhang, K.; Dai, Y.; Zhou, Z.; Jan, S. U.; Guo, L.; Gong, J. R. Polarization-Induced Saw-Tooth-Like Potential Distribution in Zincblende-Wurtzite Superlattice for Efficient Charge Separation. *Nano Energy* **2017**, *41*, 101−108.

(53) Blank, H.; Delavignette, P.; Amelinckx, S. Dislocations and Wide Stacking Faults in Wurtzite Type Crystals: Zinc Sulfide and Aluminium Nitride. *Phys. Status Solidi B* **1962**, *2*, 1660−1669.

(54) Takeuchi, S.; Suzuki, K.; Maeda, K.; Iwanaga, H. Stacking-Fault Energy of II−VI Compounds. *Philos. Mag. A* **1985**, *2*, 171−178.

(55) Heine, V.; Cheng, C. The Origin of Polytypes in SiC and ZnS. *Geometry and Thermodynamics*; NATO ASI Series; Springer: Boston, 1990; pp 311−322.

(56) Boutaiba, F.; Belabbes, A.; Ferhat, M.; Bechstedt, F. Polytypism in ZnS, ZnSe, and ZnTe: First-Principles Study. *Phys. Rev. B: Condens. Matter Mater. Phys.* **2014**, *24*, 245308.

(57) Engel, G.; Needs, R. Total Energy Calculations on Zinc Sulphide Polytypes. *J. Phys.: Condens. Matter* **1990**, *2*, 367.

(58) Miura, M.; Murata, H.; Shiro, Y.; Iishi, K. Ionicity Scale and Piezoelectricity of Crystals with Zincblende-and Wurtzite-Type Structure. *J. Phys. Chem. Solids* **1981**, *42*, 931−936.

(59) Kozielski, M. J. Dependence of Hexagonal Layer Formation in ZnS Crystals on Dopant Concentration. *Bull. Acad. Polym. Sci.: Ser. Mat. Astr. Phys.* **1978**, *26*, 353−359.

(60) Knitter, S.; Binnewies, M. Chemical Vapor Transport of Solid Solutions. Part 5. Chemical Transport of MnS/ZnS, FeS/ZnS, and FeS/MnS Mixed Crystals. *Z. Anorg. Allg. Chem.* **1999**, *625*, 1582−1588.

(61) Prenitzer, B.; Urbanik-Shannon, C.; Giannuzzi, L.; Brown, S.; Irwin, R.; Shofner, T.; Stevie, F. The Correlation between Ion Beam/Material Interactions and Practical FIB Specimen Preparation. *Microsc. Microanal.* **2003**, *9*, 216−236.

(62) Volkert, C. A.; Minor, A. M. Focused Ion Beam Microscopy and Micromachining. *MRS Bull.* **2007**, *32*, 389−399.

(63) Stevens-Kalceff, M. A. Kelvin Probe Microscopy of Localized Electric Potentials Induced in Insulating Materials by Electron Irradiation. *Microsc. Microanal.* **2004**, *10*, 797−803.

(64) Stevens-Kalceff, M.; Kruss, D. Focused Ion Beam Induced Local Modifications of the Contact Potential Difference of *n*- and *p*-Doped Silicon. *J. Phys. D: Appl. Phys.* **2009**, *42*, 145117.

(65) Zhou, Z.; Li, M.; Wu, P.; Guo, L. Revisiting the Zinc-Blende/Wurtzite Heterocrystalline Structure in CdS. *Adv. Condens. Matter Phys.* **2014**, *2014*, 1.

(66) Sharma, R.; Bisen, D. P.; Chandra, B. P. Experimental and Theoretical Study of the Mechanoluminescence of ZnS:Mn Nanoparticles. *J. Electron. Mater.* **2015**, *44*, 3312−3321.

(67) Scarmozzino, R. Effects of Hydrostatic Pressure on Triboluminescent Materials. *Solid State Commun.* **1971**, *9*, 1159−1162.

(68) Wang, X.; Peng, D.; Huang, B.; Pan, C.; Wang, Z. L. Piezophotonic Effect Based on Mechanoluminescent Materials for

Advanced Flexible Optoelectronic Applications. *Nano Energy* **2019**, *55*, 389−400.

(69) Bringuier, E. High-Field Conduction in Semi-Insulating ZnS Films. *Philos. Mag. B* **1997**, *75*, 209−228.

(70) Streetman, B. G.; Banerjee, S. *Solid State Electronic Devices*, 6th ed.; Prentice Hall Series in Solid State Physical Electronics; Pearson/Prentice Hall: New Delhi, 2006; pp 61−250.

(71) Shachar, G.; Brada, Y.; Alexander, E.; Yacobi, Y. Electroabsorption and Internal Fields in ZnS Crystals. *J. Appl. Phys.* **1970**, *41*, 723−728.

(72) Suyver, J.; Wuister, S.; Kelly, J.; Meijerink, A. Synthesis and Photoluminescence of Nanocrystalline ZnS:Mn^{2+}. *Nano Lett.* **2001**, *1*, 429−433.

(73) Murayama, M.; Nakayama, T. Chemical Trend of Band Offsets at Wurtzite/Zinc-Blende Heterocrystalline Semiconductor Interfaces. *Phys. Rev. B: Condens. Matter Mater. Phys.* **1994**, *49*, 4710.

(74) Zubko, P.; Catalan, G.; Tagantsev, A. K. Flexoelectric Effect in Solids. *Annu. Rev. Mater. Res.* **2013**, *43*, 387−421.

(75) Yang, Q.; Wang, W.; Xu, S.; Wang, Z. L. Enhancing Light Emission of ZnO Microwire-Based Diodes by Piezo-Phototronic Effect. *Nano Lett.* **2011**, *11*, 4012−4017.

(76) Pelant, I.; Valenta, J. *Luminescence Spectroscopy of Semiconductors*; Oxford University Press: New York, 2012; p 98 ff.

(77) Hoshina, T.; Kawai, H. Luminescence Excitation Spectra and Their Exciton Structures of ZnS Phosphors. I. Mn,(Cu, Al), (Ag, Al) and (Au, Al) Doped Phosphors. *Jpn. J. Appl. Phys.* **1980**, *19*, 267.

(78) Young, W. C.; Budynas, R. G. *Roark's Formulas for Stress and Strain*, 8th ed.; McGraw-Hill: New York, 2012; pp 445−548.

(79) Virkar, Y. *Software Package for Statistical Analysis of Binned Data*, v. 1.0.1; Aaron Clauset [Online], 2014. http://tuvalu.santafe.edu/~aaronc/powerlaws/bins/plbinnedcode_v1.0.1-2015-06-08.zip (retrieved July 11, 2020).

(80) Mukhina, M. *Kolmogorov - Smirnov Test of the Goodness-of-Fit*, v. 1.0.1; MATLAB Central File Exchange [Online], 2020. https://www.mathworks.com/matlabcentral/fileexchange/78038-kolmogorov-smirnov-test-of-the-goodness-of-fit (retrieved July 11, 2020).

(81) Klinger, M. More Features, More Tools, More CrysTBox. *J. Appl. Crystallogr.* **2017**, *50*, 1226−1234.